Sequestration of carbon in the deep Atlantic during the last glaciation

J. Yu[1]*, L. Menviel[2,3], Z.D. Jin[4], D.J.R. Thornalley[5], S. Barker[6], G. Marino[1], E.J. Rohling[1,7], Y. Cai[4], F. Zhang[4], X. Wang[8], Y. Dai[1], P. Chen[1,10], W.S. Broecker[9]

[1]Research School of Earth Sciences, The Australian National University, Canberra, ACT 2601, Australia

[2]Climate Change Research Centre, University of New South Wales, Sydney, Australia

[3]ARC Centre of Excellence for Climate System

[4]State Key Laboratory of Loess and Quaternary Geology, Institute of Earth Environment, Chinese Academy of Sciences, Xi'an 710075, China

[5]Dept. Of Geography, University College London, London, UK

[6]School of Earth and Ocean Sciences, Cardiff University, Cardiff, UK.

[7]Ocean and Earth Science, University of Southampton, National Oceanography Centre, Southampton SO14 3ZH, UK

[8]Earth Observatory of Singapore, Nanyang Technological University, 50 Nanyang Av., 639798, Singapore

[9]Lamont-Doherty Earth Observatory of Columbia University, 61 Route 9W/PO Box 1000, Palisades, NY, 10964-8000, USA

[10]School of Resources and Environmental Sciences, East China Normal University, Shanghai, 200062, China

*Correspondence to: jimin.yu@anu.edu.au

Atmospheric CO_2 concentrations declined markedly about 70,000 years ago, when the Earth's climate descended into the last ice age[1,2]. Much of the carbon removed from the atmosphere has been suspected to have entered the deep oceans[3,4], but evidence for increased carbon storage remains elusive. Here we use the B/Ca ratios of benthic foraminifera from several sites across the Atlantic Ocean to reconstruct changes in the carbonate ion concentration and hence the carbon inventory of the deep Atlantic across

this transition. We find that deep Atlantic carbonate ion concentration declined by around 25 μmol kg^{-1} between ~80,000 and 65,000 years ago. This drop implies that the deep Atlantic carbon inventory increased by at least 50 Gt around the same time as the amount of atmospheric carbon dropped by about 60 Gt. From a comparison with proxy records of deep circulation and climate model simulations[5], we infer that the carbon sequestration coincided with a shoaling of the Atlantic meridional overturning circulation. We thus conclude that changes in the Atlantic ocean circulation may have played an important role in reductions of atmospheric CO_2 concentrations during the last glaciation, by increasing the carbon storage in the deep Atlantic.

Ice-core records show a tight correlation between changes in atmospheric CO_2 and Antarctic temperature, suggesting an important impact of atmospheric CO_2 fluctuations on Earth's climate on orbital and millennial timescales[1,2]. During the last glacial cycle, a major climate change occurred at the Marine Isotope Stage (MIS) 5-4 transition around 70 thousand years ago (ka), with significant global cooling, substantial build-up of polar ice-sheets, and profound ocean circulation changes[2,6-9]. The atmospheric CO_2 decline across this transition accounts for about one-third of the entire interglacial-glacial atmospheric CO_2 drawdown[1,2]. Although the deep ocean is the widely suspected culprit for lowering glacial atmospheric CO_2[3,4], through biogeochemical and physical processes[5,8,10,11], convincing evidence for carbon sequestration in the deep ocean is limited[12,13], and the role of ocean circulation changes in deep-sea carbon storage remains elusive[5,8]. Here, we quantify carbon budget change in the deep

Atlantic and investigate its relationship with changes in the Atlantic Meridional Ocean Circulation (AMOC) across the MIS 5-4 transition.

Seawater carbonate ion concentration ($[CO_3^{2-}]$) is primarily governed by dissolved inorganic carbon (DIC) and alkalinity (ALK) (Fig. 1); other parameters such as temperature and salinity only play minor roles when ALK and DIC remain unchanged[14,15]. Changes (Δ) in $[CO_3^{2-}]$, DIC and ALK can be approximated by

$$\Delta_{[CO_3^{2-}]} \approx k \times (\Delta_{ALK} - \Delta_{DIC}) \qquad (1)$$

where $k = 0.59 \pm 0.01$ (1σ; used throughout) (Supplementary Fig. 1, 2). Therefore, with sound knowledge about Δ_{ALK}, reconstructions of deep-water $\Delta_{[CO_3^{2-}]}$ allow an estimate of Δ_{DIC}, the term that ultimately determines the carbon budget change of the investigated ocean reservoir. Equation (1) successfully predicts DIC in the preindustrial deep Atlantic Ocean[16] (Fig. 1b).

Deep Atlantic $[CO_3^{2-}]$ reconstructions

We present deep-water $[CO_3^{2-}]$ during ~90-50 ka for 10 sediment cores (6 new and 4 from ref. [17,18]) from a wide geographic and depth range in the Atlantic Ocean (Fig. 1). Deep-water $[CO_3^{2-}]$ is reconstructed using B/Ca in the epifaunal benthic foraminifer *Cibicidoides wuellerstorfi*, with an uncertainty of ±5 μmol kg^{-1} for $[CO_3^{2-}]$ from core-top calibration[19] (Supplementary Fig. 3). Sediment-core age models are constructed by tuning all benthic $\delta^{18}O$ records to the LR04 $\delta^{18}O$ stack[20] (Supplementary Fig. 4-6 and Table 1-3). The age ranges for MIS 5a (85-75 ka) and MIS 4 (59-69 ka) are based on light (<~3.3‰) and heavy (>~3.8‰) benthic $\delta^{18}O$ values, respectively.

Fig. 2 shows that *C. wuellerstorfi* B/Ca decreased from MIS 5a to MIS 4 in all 10 cores. Relative to mean MIS 5a, deviations of B/Ca ($\Delta_{B/Ca}$) during MIS 4 are -20±5 μmol mol^{-1} (n=35) in 7 cores from the eastern basin and -42±11 μmol mol^{-1} (n=21) in 3 cores (EW9209-2JPC, RC16-59, and GeoB1118-3) from the western Atlantic (Fig. 3a-b; Supplementary Table 4). Because *C. wuellerstorfi* B/Ca is minimally biased by postmortem dissolution[19,21], we attribute decreased MIS 4 B/Ca values to reductions in deep-water [CO_3^{2-}]. Using a core-top derived sensitivity of 1.14 μmol mol^{-1} per μmol kg^{-1} specific to *C. wuellerstorfi*[19], benthic $\Delta_{B/Ca}$ suggest 18±6 and 37±12 μmol kg^{-1} [CO_3^{2-}] reductions in the eastern and western basins, respectively (Fig. 3a). Considering all 10 cores, benthic B/Ca decreased by 28±13 μmol mol^{-1} (n=56), corresponding to a 25±13 μmol kg^{-1} decline in [CO_3^{2-}], from MIS 5a to MIS 4 (Fig. 3).

Different from $\Delta_{B/Ca}$, benthic $\delta^{13}C$ amplitudes are similar between cores at ~3.5 km water depth from the eastern (MD01-2446 and MD95-2039) and western (EW9209-2JPC and RC16-59) North Atlantic (Supplementary Fig. 7). One possibility for this contrast is different $\delta^{13}C$ endmembers in the source waters ventilating the two basins during MIS 4. $\delta^{13}C$ heterogeneity of northern sourced waters has been reported for the Last Glacial Maximum[14,22]. We here attribute the larger $\Delta_{B/Ca}$ to a greater ocean circulation change in the western basin (Supplementary Fig. 8), necessitating a higher source-water $\delta^{13}C$ for the western Atlantic during MIS 4. Future work is required to validate this, but the associated uncertainties do not affect our conclusions.

Benthic B/Ca and $\delta^{18}O$ are negatively correlated in each core (Supplementary Fig. 9-10). This suggests that the decrease in deep-water [CO_3^{2-}] into MIS 4 was associated with deep-sea cooling and continental ice buildup, which are thought to be linked to declining atmospheric CO_2

during glaciation[1,2,6,23]. The overall pattern of deep-water [CO_3^{2-}] changes, identified through Monte-Carlo-style probabilistic assessment of the combined [CO_3^{2-}] reconstructions for our 10 cores, displays a first-order similarity to the evolution of atmospheric CO_2, in that both deep Atlantic [CO_3^{2-}] and atmospheric CO_2 decreased from MIS 5a to MIS 4[1,2] (Fig. 3c, d). This provides evidence to support previous suggestions[11,14,18,24] that changes in deep Atlantic carbonate chemistry played an important role in glacial-interglacial atmospheric CO_2 variations.

Because our data are from 10 sites widely distributed in the Atlantic (water depth: ~2.9-5 km, latitude: 41°S-41°N) (Fig. 1), we consider that the 25±13 μmol kg^{-1} reduction in deep-water [CO_3^{2-}] approximates the mean [CO_3^{2-}] change in the entire deep Atlantic (>~3 km) from MIS 5a to 4 (Fig. 3a-c). As a cross-check, we use the [CO_3^{2-}]-$\delta^{13}C$ relationship and the mean deep Atlantic $\delta^{13}C$ change to infer the mean deep Atlantic [CO_3^{2-}] decrease across the MIS 5a-4 transition (Supplementary Fig. 11-12). In our 10 cores, deep-water [CO_3^{2-}] is significantly correlated with benthic $\delta^{13}C$ (r^2=0.50, P<0.0001), yielding a slope of 0.0228‰ per μmol kg^{-1}. A previous compilation study has revealed an average decline of ~0.45‰ in benthic $\delta^{13}C$ throughout the deep Atlantic from MIS 5a to MIS 4[25]. If the [CO_3^{2-}]-$\delta^{13}C$ relationship observed at our 10 geographically widely distributed sites is applicable to other locations in the deep Atlantic, a 0.45‰ drop in $\delta^{13}C$ suggests a ~20 μmol kg^{-1} reduction in deep-water [CO_3^{2-}], falling within the uncertainty of 25±13 μmol kg^{-1} calculated from our [CO_3^{2-}] reconstructions (Fig. 3a-c).

Quantifying carbon sequestration

Equation (1) indicates that changes in $[CO_3^{2-}]$ depend on variations in ALK and DIC. Four lines of evidence suggest that the lowered deep-water $[CO_3^{2-}]$ during MIS 4 was not caused by an ALK drop, but by an increase in deep Atlantic DIC. First, when $[CO_3^{2-}]$ declines, deep water becomes more corrosive and that would enhance water-column and deep-sea $CaCO_3$ dissolution, a process that drives up oceanic ALK[4,14]. This was illustrated in the preindustrial Atlantic, where the $[CO_3^{2-}]$ decrease from North Atlantic Deep Water (NADW) to Antarctic Bottom Water (AABW) was accompanied by an ALK rise (Fig. 1d)[16]. Our studied cores (Fig. 2) and many other locations in the deep Indo-Pacific[26-28] show intensified deep-sea $CaCO_3$ dissolution during the MIS 5a-4 transition, with a likely effect of raising the global oceanic ALK inventory[4,14]. Second, the ~50 m sea level drop into MIS 4[6] would have substantially reduced the shelf area for neritic carbonate deposition, which in turn would have raised oceanic ALK[29]. Third, benthic Ba/Ca ratios, a proxy for deep-water ALK[30], show some sign of increase during MIS 4 at four locations in the Atlantic (Supplementary Fig. 13). Fourth, model studies suggest higher ocean ALK in glacials than in interglacials[11,31].

To quantify the magnitude of deep-water DIC increase (Fig. 3b; Supplementary Information), we first assume no change in ALK (i.e., $\Delta_{ALK} = 0$), and subsequently evaluate how this assumption affects the conclusions. Based on Equation (1), a 25±13 μmol kg^{-1} decline in deep-water $[CO_3^{2-}]$ translates into a 42±22 μmol kg^{-1} increase in DIC. Using a mass of 10.1×10^{19} kg for waters below 3 km in the Atlantic, we calculate that a total amount of 51±27 Gt extra carbon was sequestered in the deep Atlantic during the MIS 5a-4 transition (Fig. 3c). During this period, atmospheric CO_2 declined by 28±11 ppm (MIS 5a: 237±8 ppm; MIS 4: 208±8 ppm), corresponding to a loss of 60±23 Gt carbon from the atmosphere[1,2] (Fig. 3d). Therefore, the

carbon stock increase in the deep Atlantic is, in quantity, equivalent to ~86±56% of the concurrent atmospheric CO_2 drawdown across the MIS 5a-4 transition.

Note that the deep Atlantic carbon budget change calculated above likely represents a conservative estimate due to a possible rise in the global ocean ALK. CO_2 sequestration in the deep ocean across MIS 5a-4 would inevitably raise deep-water acidity, lower seawater [CO_3^{2-}], and consequently intensify deep-sea $CaCO_3$ dissolution (Fig. 2). By raising the whole ocean ALK, the so-called deep-sea carbonate compensation (Supplementary Information) serves as a negative feedback to restore the global deep-water [CO_3^{2-}] to levels at which the global ocean ALK input (mainly from continental weathering) reaches a new steady state with ALK output (by shelf and deep-sea carbonate burial)[4,14,21,32-34]. The effect of carbonate compensation may be manifested by partial reversals of [CO_3^{2-}] in MD01-2446, EW9209-2JPC, and RC16-59 (Fig. 2). However, none of the studied [CO_3^{2-}] records returned to the MIS 5a levels within the ~10,000-year duration of MIS 4, compared to the relaxation timescale of ~5-7,000 years associated with carbonate compensation[32]. Nevertheless, deep Atlantic [CO_3^{2-}] results shown in Fig. 3b cannot be treated as the global mean changes, for which [CO_3^{2-}] variations in the deep Indo-Pacific have to be taken into account[33]. Considering the increased $CaCO_3$ burial and [CO_3^{2-}] in the deep Pacific during the latter phase of MIS 4[35,36], the steady-state global mean deep-water [CO_3^{2-}] might remain roughly stable from MIS 5a to MIS 4, consistent with previous modeling work[33,37]. Because there was increased carbon sequestration in the glacial deep ocean[3,4,11,12], a relatively stable deep-sea [CO_3^{2-}] would suggest a greater ALK inventory during MIS 4. Alternatively, reduced weathering (perhaps induced by cold-dry glacial climates[32]) coupled with a weakening or shutdown of NADW can also maintain deep Atlantic [CO_3^{2-}] at low values for ~8,000 years

without invoking a global ALK change, as shown by models (Supplementary Fig. 15, 19). These scenarios are not mutually exclusive and are both consistent with the carbonate compensation theory. Insufficient evidence is available to reject either scenario, but a large change in weathering may not be expected given an opposing effect from the exposure of shelves[6] that tends to enhance carbonate weathering[38]. If global weathering remained roughly constant, then the global ocean ALK would have been higher during MIS 4 than during MIS 5a. Without a global ALK increase due to carbonate compensation, a much larger $[CO_3^{2-}]$ decrease would be expected in the deep Atlantic during MIS 4.

Given a deep-water $[CO_3^{2-}]$ reduction, Equation (1) suggests that for every unit increase in ALK the DIC increase would be one unit higher than the number calculated assuming $\Delta_{ALK} = 0$. This is demonstrated by distributions of carbon species in today's Atlantic Ocean (Fig. 1)[16]: to account for the ~40 μmol kg^{-1} $[CO_3^{2-}]$ reduction between NADW ($[CO_3^{2-}]$ = ~120 μmol kg^{-1}) and AABW ($[CO_3^{2-}]$ = ~80 μmol kg^{-1}), Equation (1) would predict a $\Delta_{DIC_{AABW-NADW}}$ of ~68 μmol kg^{-1} without any change in ALK, which is ~38% smaller than the observed DIC change (Fig. 1c). The difference is caused by a ~40 μmol kg^{-1} ALK increase from NADW to AABW (Fig. 1d). Had the pre-industrial $\Delta_{[CO_3^{2-}]}$:Δ_{DIC} ratio of -0.37 been applied, which empirically includes the ALK changes (Fig. 1c), then our calculated deep Atlantic carbon storage increase would be amplified by a factor of 1.6, and the quantity of carbon sequestration in the deep Atlantic would be comparable (within uncertainties) to the entire atmospheric CO_2 decline from MIS 5a to MIS 4. Additionally, consideration of larger $\Delta_{B/Ca}$ in the western Atlantic, which is currently under-sampled (Fig. 3a), would potentially raise the estimate of carbon sequestration in the deep Atlantic.

Reasons for carbon sequestration

Enhanced carbon storage in the deep Atlantic during MIS 4 may have resulted from a synergy of physical and biogeochemical processes[4,11]. Regarding physical processes, sediment neodymium isotopes (εNd; an ocean circulation proxy) imply an increased contribution of CO_2-rich southern-sourced abyssal waters (Fig. 1) in the deep Atlantic at the MIS 5a-4 transition[5,39]. During MIS 4, the NADW-AABW boundary probably shoaled to ~2-3 km water depth, and was located above major topographic ridges and seamounts[8,39]. Such an AMOC rearrangement would weaken diapycnal mixing between water masses, enhance water-column stratification, and thereby facilitate the retention of sequestered carbon in the deep ocean[7,40]. In core TNO57-21, a sharp ~1ε unit increase in εNd at ~70 ka[5] exactly coincided with a rapid ~12 μmol kg^{-1} decline in deep-water [CO_3^{2-}] (Fig. 4). Because seawater [CO_3^{2-}] is primarily determined by DIC and ALK, both of which place direct constraints on the oceanic carbon cycle[4,11,32,34], synchronous changes in εNd and [CO_3^{2-}] indicate a tight coupling between AMOC and carbon cycling in the deep Atlantic during the last glaciation. An ~0.5‰ decrease in benthic $\delta^{13}C$ (Fig. 4b)[41] at ~72 ka was previously interpreted to reflect a global carbon budget change to pre-date an AMOC reorganization[5]. Were this $\delta^{13}C$ decline caused by carbon transfer from land biosphere[5], it would concomitantly decrease deep-water [CO_3^{2-}] and intensify deep-sea $CaCO_3$ dissolution, a phenomenon not observed in TNO57-21 (Fig. 2f, 4). Instead, we contend that the $\delta^{13}C$ decline might reflect processes like air-sea isotopic exchange[42]. The coupling of AMOC and carbon cycling is further corroborated by results from two Earth system models of intermediate complexity: halving NADW formation leads to 10-30 μmol kg^{-1} reductions in [CO_3^{2-}] below ~3 km in the deep Atlantic without causing deep-sea anoxia (Supplementary Fig. 22-23).

Additionally, cooler climate during MIS 4 would raise CO_2 solubility and preformed DIC of deep waters[13,43], enhancing CO_2 sequestration in the deep ocean. Regarding the biogeochemistry, the decreased deep Atlantic [CO_3^{2-}] during MIS 4 is consistent with greater water-column remineralization due to reduced vertical mixing associated with a shoaled AMOC[8,9,39,44] and a more efficient biological pump in the glacial Southern Ocean perhaps stimulated by increased iron availability[10], both of which would increase sequestration of respiratory DIC into the ocean interior and decrease atmospheric CO_2[4,11,45,46] (Supplementary Fig. 25).

Overall, our calculations highlight that, despite its relatively modest proportion (~30%) of the global deep ocean volume, the deep Atlantic sequestered a substantial amount of carbon during the last glaciation at ~70 ka. The sequestered amount is quantitatively comparable to the contemporary carbon loss from the atmosphere. We also find that this large carbon sequestration was tightly coupled with AMOC changes. The movements of carbon between reservoirs in the atmosphere-land biosphere-ocean system are intricately linked, and future studies may aim to quantify the contributions from individual sources to the increased carbon storage in the deep ocean during glaciations.

Methods

Methods and any associated references are available in the online version of the paper.

References

1. Ahn, J. & Brook, E. J. Atmospheric CO(2) and climate on millennial time scales during the last glacial period. *Science* **322**, 83-85 (2008).

2. Bereiter, B. et al. Mode change of millennial CO2 variability during the last glacial cycle associated with a bipolar marine carbon seesaw. *Proceedings of the National Academy of Sciences of the United States of America* **109**, 9755-9760 (2012).
3. Broecker, W. Glacial to interglacial changes in ocean chemistry. *Progr. Oceanogr.* **2**, 151-197 (1982).
4. Sigman, D. M. & Boyle, E. A. Glacial/interglacial variations in atmospheric carbon dioxide. *Nature* **407**, 859-869 (2000).
5. Piotrowski, A., Goldstein, S. J., Hemming, S. R. & Fairbanks, R. G. Temporal Relationships of carbon cycling and ocean circulation at glacial boundaries. *Science* **307**, 1933-1938 (2005).
6. Grant, K. M. et al. Rapid coupling between ice volume and polar temperature over the past 150,000 years. *Nature*, doi:10.1038/nature11593 (2012).
7. Adkins, J. F. The role of deep ocean circulation in setting glacial climates. *Paleoceanography* **28**, 539-561 (2013).
8. Thornalley, D. J. R., Barker, S., Becker, J., Hall, I. R. & Knorr, G. Abrupt changes in deep Atlantic circulation during the transition to full glacial conditions. *Paleoceanography* **28**, 253-262 (2013).
9. Barker, S. & Diz, P. Timing of the descent into the last ice age determined by the bipolar seesaw. *Paleoceanography* (2014).
10. Martinez-Garcia, A. et al. Iron Fertilization of the Subantarctic Ocean During the Last Ice Age. *Science* **343**, 1347-1350 (2014).
11. Hain, M. P., Sigman, D. M. & Haug, G. H. Carbon dioxide effects of Antarctic stratification, North Atlantic Intermediate Water formation, and subantarctic nutrient drawdown during the last ice age: Diagnosis and synthesis in a geochemical box model. *Global Biogeochemical Cycles* **24** (2010).
12. Hoogakker, B. A. A., Elderfield, H., Schmiedl, G., McCave, I. N. & Rickaby, R. E. M. Glacial-interglacial changes in bottom-water oxygen content on the Portuguese margin. *Nature Geoscience* **8**, 40-43 (2015).
13. Goodwin, P. & Lauderdale, J. M. Carbonate ion concentrations, ocean carbon storage, and atmospheric CO2. *Global Biogeochemical Cycles* **27**, 882-893 (2013).
14. Yu, J. M., Elderfield, H. & Piotrowski, A. Seawater carbonate ion-$\delta^{13}C$ systematics and application to glacial-interglacial North Atlantic ocean circulation. *Earth and Planetary Science Letters* **271**, 209-220. doi:10.1016/j.epsl.2008.04.010 (2008).
15. Zeebe, R. E. & Wolf-Gladrow, D. A. *CO_2 in Seawater: Equilibrium, Kinetics, Isotopes* (ed. Halpern, D.) (Elsevier, Amsterdam, 2001).
16. Key, R. M. et al. A global ocean carbon climatology: Results from Global Data Analysis Project (GLODAP). *Global Biogeochemical Cycles* **18** (2004).
17. Broecker, W., Yu, J. & Putnam, A. E. Two contributors to the glacial CO_2 decline. *Earth and Planetary Science Letters*, http://dx.doi.org/10.1016/j.epsl.2015.07.019 (2015).
18. Raitzsch, M., Hathorne, E. C., Kuhnert, H., Groeneveld, J. & Bickert, T. Modern and late Pleistocene B/Ca ratios of the benthic foraminifer Planulina wuellerstorfi determined with laser ablation ICP-MS. *Geology* **39**, 1039-1042 (2011).
19. Yu, J. M. & Elderfield, H. Benthic foraminiferal B/Ca ratios reflect deep water carbonate saturation state. *Earth and Planetary Science Letters* **258**, 73-86, doi: 10.1016/j.epsl.2007.03.025 (2007).

20. Lisiecki, L. E. & Raymo, M. E. A Pliocene-Pleistocene stack of 57 globally distributed benthic $\delta^{18}O$ records. *Paleoceanography* **20**, PA1003, doi:10.1029/2004PA001071 (2005).
21. Yu, J. et al. Deep South Atlantic carbonate chemistry and increased interocean deep water exchange during last deglaciation. *Quaternary Science Reviews* (2014).
22. Repschlager, J., Weinelt, M., Andersen, N., Garbe-Schonberg, D. & Schneider, R. Northern source for Deglacial and Holocene deepwater composition changes in the Eastern North Atlantic Basin. *Earth and Planetary Science Letters* **425**, 256-267 (2015).
23. Elderfield, H. et al. Evolution of Ocean Temperature and Ice Volume Through the Mid-Pleistocene Climate Transition. *Science* **337**, 704-709 (2012).
24. Hodell, D. A., Charles, C. D. & Sierro, F. J. Late Pleistocene evolution of the ocean's carbonate system. *Earth and Planetary Science Letters* **192**, 109-124 (2001).
25. Oliver, K. I. C. et al. A synthesis of marine sediment core delta C-13 data over the last 150 000 years. *Climate of the Past* **6**, 645-673 (2010).
26. Le, J. & Shackleton, N. J. Carbonate dissolution fluctuations in the Western equatorial Pacific during the late Quaternary. *Paleoceanography* **7**, 21-42 (1992).
27. Howard, W. R. & Prell, W. L. Late Quaternary $CaCO_3$ production and preservation in the Southern Ocean - Implications for oceanic and atmospheric carbon cycling. *Paleoceanography* **9**, 453-482 (1994).
28. Lyle, M. et al. in *Proceedings of the Ocean Drilling Program, Scientific Results* (eds. Lyle, M., Koizumi, I., Richter, C. & Moore, T. C.) 163-182 (2000).
29. Ridgwell, A. J., Watson, A. J., Maslin, M. A. & Kaplan, J. O. Implications of coral reef buildup for the controls on atmospheric CO_2 since the Last Glacial Maximum. *Paleoceanography* **18** (2003).
30. Lea, D. & Boyle, E. Barium content of benthic foraminifera controlled by bottom- water composition. *Nature* **338**, 751-753 (1989).
31. Toggweiler, J. R. Origin of the 100,000-year timescale in Antarctic temperatures and atmospheric CO_2. *Paleoceanography* **23**, PA2211, doi:10.1029/2006PA001405 (2008).
32. Broecker, W. S. & Peng, T. H. The role of $CaCO_3$ compensation in the glacial to interglacial atmospheric CO_2 change. *Global Biogeochemical Cycles* **1**, 15-29 (1987).
33. Emerson, S. & Archer, D. Glacial carbonate dissolution cycles and atmospheric pCO_2: A view from the ocean bottom. *Paleoceanography* **7**, 319-331 (1992).
34. Marchitto, T. M., Lynch-Stieglitz, J. & Hemming, S. R. Deep Pacific $CaCO_3$ compensation and glacial-interglacial atmospheric CO_2. *Earth and Planetary Science Letters* **231**, 317-336 (2005).
35. Anderson, R. F., Fleisher, M. Q., Lao, Y. & Winckler, G. Modern $CaCO_3$ preservation in equatorial Pacific sediments in the context of late-Pleistocene glacial cycles. *Marine Chemistry* **111**, 30-46. doi:10.1016/j.marchem.2007.11.011 (2008).
36. Yu, J. et al. Responses of the deep ocean carbonate system to carbon reorganization during the Last Glacial–interglacial cycle. *Quaternary Science Reviews* **76**, 39-52 (2013).
37. Boyle, E. The role of vertical chemical fractionation in controlling late Quaternary atmospheric carbon dioxide. *J. Geophys. Res.* **93**, 15701-15714 (1988).
38. Gibbs, M. T. & Kump, L. R. Global chemical erosion during the last glacial maximum and the present: Sensitivity to changes in lithology and hydrology. *Paleoceanography* **9**, 529-543 (1994).

39. Bohm, E. et al. Strong and deep Atlantic meridional overturning circulation during the last glacial cycle. *Nature* **517**, 73-U170 (2015).
40. Ferrari, R. et al. Antarctic sea ice control on ocean circulation in present and glacial climates. *Proceedings of the National Academy of Sciences of the United States of America* **111**, 8753-8758 (2014).
41. Ninnemann, U. S. & Charles, C. D. Changes in the mode of Southern Ocean circulation over the last glacial cycle revealed by foraminiferal stable isotopic variability. *Earth And Planetary Science Letters* **201**, 383-396 (2002).
42. Lynch-Stieglitz, J., Stocker, T. F., Broecker, W. & Fairbanks, R. G. The influence of air-sea exchange on the isotopic composition of oceanic carbon: Observations and modeling. *Global Biogeochemical Cycles* **9**, 653-665 (1995).
43. Williams, R. G. & Follows, M. J. *Ocean Dynamics and the Carbon Cycle: Principals and Mechanisms* (Cambridge Univ. Press, Cambridge, U.K. , 2011).
44. Menviel, L., England, M. H., Meissner, K. J., Mouchet, A. & Yu, J. Atlantic-Pacific seesaw and its role in outgassing CO2 during Heinrich events. *Paleoceanography* **29**, 58-70 (2014).
45. Menviel, L., Joos, F. & Ritz, S. P. Simulating atmospheric CO_2, ^{13}C and the marine carbon cycle during the Last Glacial/Interglacial cycle: possible role for a deepening of the mean remineralization depth and an increase in the oceanic nutrient inventory. *Quaternary Science Reviews* **56**, 46-68 (2012).
46. Menviel, L., Spence, P. & England, M. H. Contribution of enhanced Antarctic Bottom Water formation to Antarctic warm events and millennial-scale atmospheric CO2 increase. *Earth and Planetary Science Letters* **413**, 37-50 (2015).
47. Schlitzer, R. Ocean Data View. **http://odv.awi-bremerhaven.de** (2006).
48. Weaver, A. J. et al. The UVic Earth System Climate Model: Model description, climatology, and applications to past, present and future climates. *Atmosphere-Ocean* **39**, 361-428 (2001).
49. Menviel, L., Timmermann, A., Mouchet, A. & Timm, O. Meridional reorganizations of marine and terrestrial productivity during Heinrich events. *Paleoceanography* **23** (2008).
50. Meissner, K. J., Schmittner, A., Weaver, A. J. & Adkins, J. The ventilation of the North Atlantic Ocean during the Last Glacial Maximum: A comparison between simulated and observed radiocarbon ages. *Paleoceanography* **18**, doi:10.1029/2002PA000762 (2003).
51. Yu, J. M., Elderfield, H., Greaves, M. & Day, J. Preferential dissolution of benthic foraminiferal calcite during laboratory reductive cleaning. *Geochemistry Geophysics Geosystems* **8**, Q06016, doi:10.1029/2006GC001571 (2007).
52. Barker, S., Greaves, M. & Elderfield, H. A study of cleaning procedures used for foraminiferal Mg/Ca paleothermometry. *Geochemistry Geophysics Geosystems* **4**, 8407 (2003).
53. Yu, J. M., Day, J., Greaves, M. & Elderfield, H. Determination of multiple element/calcium ratios in foraminiferal calcite by quadrupole ICP-MS. *Geochemistry Geophysics Geosystems* **6**, Q08P01, doi:10.1029/2005GC000964 (2005).
54. Boyle, E. & Keigwin, L. D. Comparison of Atlantic and Pacific paleochemical records for the Last 215,000 years: Changes in deep ocean circulation and chemical inventories. *Earth and Planetary Science Letters* **76**, 135-150 (1985/86).
55. Yu, J., Anderson, R. F. & Rohling, E. J. Deep ocean carbonate chemistry and glacial-interglacial atmospheric CO_2 changes. *Oceanography* **27**, 16-25 (2014).

56. Brown, R. E., Anderson, L. D., Thomas, E. & Zachos, J. C. A core-top calibration of B/Ca in the benthic foraminifers Nuttallides umbonifera and Oridorsalis umbonatus: A proxy for Cenozoic bottom water carbonate saturation. *Earth and Planetary Science Letters* **310**, 360-368 (2011).
57. Pelletier, G., Lewis, E. & Wallace, D. *A calculator for the CO_2 system in seawater for Microsoft Excel/VBA* (Washington State Department of Ecology, Olympia, WA, Brookhaven National Laboratory, Upton, NY, 2005).
58. Rohling, E. J. et al. Sea-level and deep-sea-temperature variability over the past 5.3 million years. *Nature* **508**, 477-+ (2014).

Acknowledgments. We thank Jerry McManus, Daniel Sigman, Bob Anderson, and three anonymous reviewers for insightful and constructive discussions and comments, and Les Kinsley and Laura Rodriguez-Sanz for laboratory assistance. This work is supported by ARC Discovery Project (DP140101393) and Future Fellowship (FT140100993) to JY, CAS/SAFEA International Partnership Program for Creative Research Teams to JY and ZJ, DECRA (DE150100107) to LM, and by Australian Laureate Fellowship (FL120100050) to EJR. Core materials were kindly provided by LDEO (Nichole Anest), NOC (Guy Rothwell), GEREGE (Nicholas Thouveny), and WHOI (Ellen Roosen/Delia Oppo) core repositories. Model experiments were performed on a computational cluster owned by the Faculty of Science of the University of New South Wales as well as on a cluster from the NCI National Facility at the Australian National University.

Author contributions. JY designed and performed the research and wrote the paper; LM carried out modeling; ZJ/FZ picked foram shells; DJRT/SB and YD/PC generated data for MD95-2039 and EW9209-2JPC/RC16-59, respectively; GM/EJR conducted MC simulation; all authors contributed to improving the manuscript.

Additional information. Supplementary information is available in the online version of the paper. Reprints and permissions information is available online at www.nature.com/reprints. Correspondence and requests for materials should be addressed to J.Y.

Competing financial interests. The authors declare no competing financial interests.

Figure 1 | **Preindustrial Atlantic Ocean carbonate chemistry and sediment cores**. **a**, Locations of studied cores (circles) against meridional DIC (color-shading) and [CO_3^{2-}] (contours, μmol kg^{-1}) transect (inset)[16,47]. Cores: a = MD95-2039, b = MD01-2446, c = EW9209-2JPC, d = RC16-59, e = GEOB1115-3, f = GEOB1117-2, g = GEOB1118-3, h = RC13-228, i = RC13-229, j = TNO57-21 (Supplementary Table 1). **b,** Predicted vs. measured DIC. **c,** DIC vs. [CO_3^{2-}]. The blue line shows the expected DIC trend based on Equation (1) when $\Delta_{ALK} = 0$ (Supplementary Information). **d,** ALK vs. [CO_3^{2-}]. Red lines (**b-d**) represent linear regressions of the deep Atlantic data (>2.5 km, 70°S-70°N, 15°E-65°W)[16].

Figure 2 | Reconstructed [CO_3^{2-}] from *C. wuellerstorfi* B/Ca in the deep Atlantic (>~3 km) during 50-90 ka. **a,** MD95-2039 (square) and MD01-2446 (circle). **b,** EW9209-2JPC (square) and RC16-59 (circle) (ref. [17] and this study). **c,** GeoB1115-3 (circle)[18], GeoB1117-2 (triangle)[18] and GeoB1118-3 (square)[18]. B/Ca from GeoB1115-3 and GeoB1118-3 are shifted by -20 and +40 μmol mol^{-1}, respectively, to facilitate plotting. The [CO_3^{2-}] scale is only for core GeoB1117-2. **d,** RC13-228. **e,** RC13-229. **f,** TNO57-21. Unless mentioned, B/Ca are from this study. Grey lines represent sediment carbonate contents (%$CaCO_3$). Shadings show MIS 5a (orange) and MIS 4 (cyan).

Figure 3 | Deep Atlantic carbon budget across the MIS 5a-4 transition. **a,** Histogram and averages (squares ±1 standard deviation) of $\Delta_{B/Ca}$ (deviations of individual measurements from the B/Ca_{MIS5a} mean) and corresponding $\Delta_{[CO_3^{2-}]}$ (upper abscissa) for MIS 5a (red) and 4 (green:

423 eastern basin; grey: western basin; black: all cores). **b,** Temporal $\Delta_{B/Ca}$ and $\Delta_{[CO_3^{2-}]}$ evolutions, with
424 minimum Δ_{DIC} calculated by Equation (1) assuming $\Delta_{ALK} = 0$. **c,** Monte-Carlo-style probabilistic
425 assessment of $[CO_3^{2-}]$ shown in **b** (curve: probability maximum; envelope: ±95% probability
426 interval). $\Delta_{\sum carbon}$ represents minimum total carbon change in the deep Atlantic; its equivalent
427 quantity in atmospheric CO_2 change is scaled by 1 ppm CO_2 = 2.1 GtC. **d,** Atmospheric CO_2[1,2].

428

429 **Figure 4 | Temporal evolution of geochemical proxies in core TNO57-21 from the deep**
430 **South Atlantic**. **a,** Sediment εNd, an ocean circulation proxy[5]. Error bars represent
431 ±1σ uncertainty. **b,** Benthic $\delta^{13}C$[41], a geochemical tracer influenced by a combination of
432 processes including ocean circulation, biogenic remineralization, and air-sea exchange, not all of
433 which are associated with a change in deep-water DIC. **c,** Benthic B/Ca (this study), a proxy for
434 deep-water $[CO_3^{2-}]$ which reflects changes in DIC and ALK, both of which are tightly linked to
435 the carbon cycle in the ocean. The high sedimentation rate (~15 cm per 1,000 years) in TNO57-
436 21 through the 65-75 ka interval significantly minimizes bioturbation influences on geochemical
437 tracers.

438

439

440 **Methods**

441 **Deep water $[CO_3^{2-}]$ vs. ALK-DIC.** Due to numerous equations and dissociation constants
442 involved in the seawater carbonate system[15], we use the Global Ocean Data Analysis Project

(GLODAP) dataset[16] and model outputs from LOVECLIM and the UVic ESCM[48-50] to explore the relationship between deep-water [CO_3^{2-}] and ALK-DIC. For the GLODAP dataset, the anthropogenic CO_2 contribution was subtracted from the measured DIC to obtain the pre-industrial values. Here we consider the deep Atlantic data (>2.5 km, 70°S-70°N, 15°E-65°W) from the GLODAP and model outputs. CO_2 system calculations are detailed in the Supplementary Information.

Core materials, analytical methods, and age model. We carried out new measurements on epibenthic (a habitat above the sediment-water interface) foraminiferal species *C. wuellerstorfi* from 7 cores. After sediments processing, benthic foraminiferal shells were picked, cleaned, and measured for $\delta^{18}O$, $\delta^{13}C$, and B/Ca following previous methods[51-54] (Supplementary Information). The analytical error in B/Ca is ~±2.5% (±3 μmol mol^{-1}), and ~0.08‰ in both $\delta^{18}O$ and $\delta^{13}C$. Age models for sediment cores are based on comparisons of benthic $\delta^{18}O$ with the LR04 stack curve[20] (Supplementary Table 2; Supplementary Fig. 4). By using one target curve for tuning, we minimize potential relative age offsets between cores.

Deep water [CO_3^{2-}] reconstruction from benthic B/Ca. To convert *C. wuellerstorfi* B/Ca into deep water [CO_3^{2-}], We use $[CO_3^{2-}]_{downcore} = [CO_3^{2-}]_{Preindustrial} + \Delta B/Ca_{downcore-coretop}/1.14$, where $[CO_3^{2-}]_{Preindustiral}$ is estimated using the GLODAP dataset[16] (Supplementary Table 1), $\Delta B/Ca_{downcore-coretop}$ represents the deviation of B/Ca of down-core samples from the core-top value, and term 1.14 denotes the sensitivity of *C. wuellerstorfi* B/Ca to deep water carbonate saturation state based on core-top calibration[18,19,36,55,56]. We quote an uncertainty of ±5 μmol kg^{-1}

464 in [CO_3^{2-}], based on the error derived from the global core-top calibration samples[19,36]. See
465 Supplementary Information for details.

466

467 **Data.** All new data presented in this study is given in Supplementary Tables.

468 **Code availability.** We have opted not to make the computer codes associated with this paper
469 available because they are based on simple Ocean Data View[47] and CO_2sys[57] data analyses and
470 established statistics[6,58].

471

472 **References:**

473 Ref 48-58 are only for Methods.

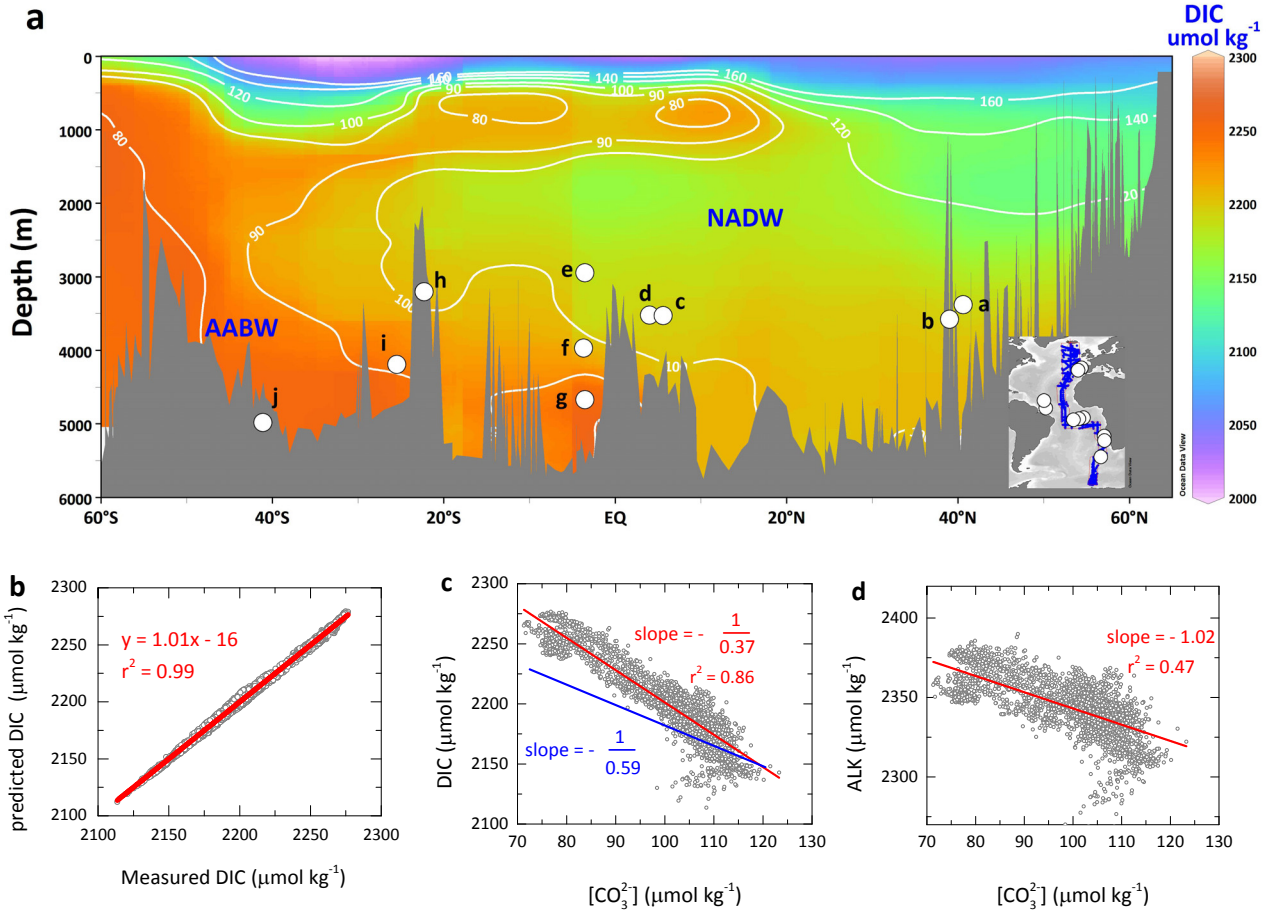
a
DIC
umol kg-1
Depth (m)
NADW
AABW
a
b
c
d
e
f
g
h
i
j
60°S
40°S
20°S
EQ
20°N
40°N
60°N
b
predicted DIC (µmol kg-1)
y = 1.01x - 16
r2 = 0.99
Measured DIC (µmol kg-1)
c
DIC (µmol kg-1)
slope = - 1/0.37
r2 = 0.86
slope = - 1/0.59
[CO32-] (µmol kg-1)
d
ALK (µmol kg-1)
slope = - 1.02
r2 = 0.47
[CO32-] (µmol kg-1)

Figure 1

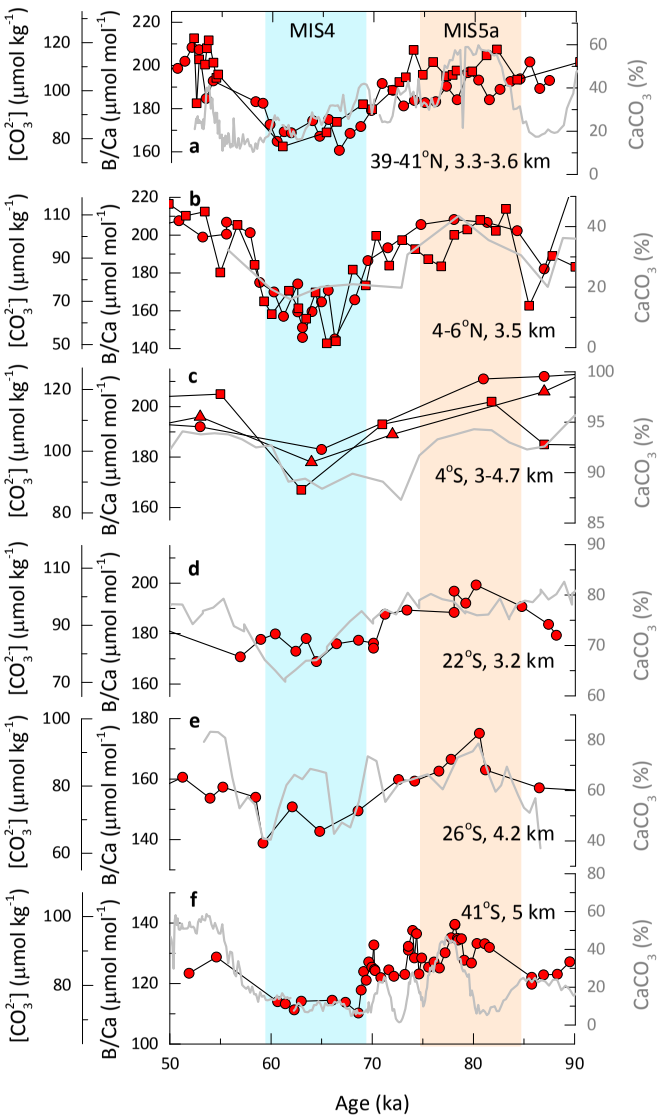
MIS4
MIS5a
a
39-41°N, 3.3-3.6 km
b
4-6°N, 3.5 km
c
4°S, 3-4.7 km
d
22°S, 3.2 km
e
26°S, 4.2 km
f
41°S, 5 km
[CO3 2-] (µmol kg-1)
B/Ca (µmol mol-1)
CaCO3 (%)
Age (ka)

Figure 2

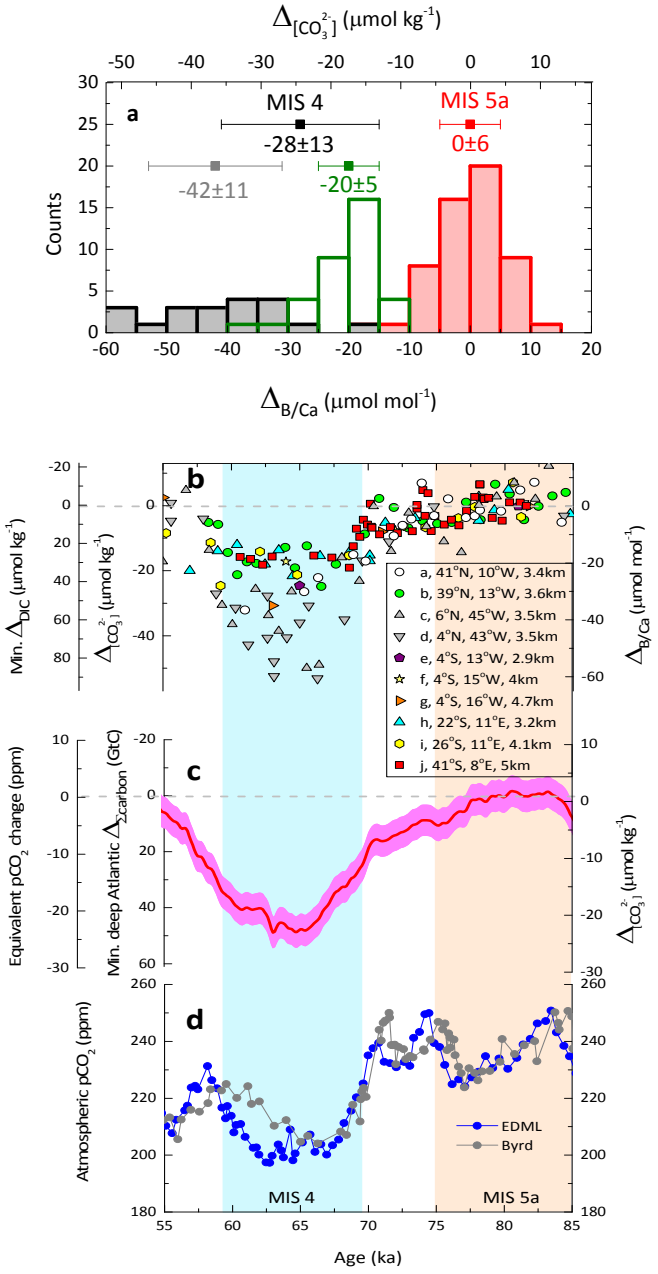
Δ[CO3 2-] (µmol kg-1)
a
MIS 4
-28±13
-42±11
-20±5
MIS 5a
0±6
Counts
ΔB/Ca (µmol mol-1)
b
Min. ΔDIC (µmol kg-1)
Δ[CO3 2-] (µmol kg-1)
ΔB/Ca (µmol mol-1)
a, 41°N, 10°W, 3.4km
b, 39°N, 13°W, 3.6km
c, 6°N, 45°W, 3.5km
d, 4°N, 43°W, 3.5km
e, 4°S, 13°W, 2.9km
f, 4°S, 15°W, 4km
g, 4°S, 16°W, 4.7km
h, 22°S, 11°E, 3.2km
i, 26°S, 11°E, 4.1km
j, 41°S, 8°E, 5km
c
Equivalent pCO2 change (ppm)
Min. deep Atlantic Δcarbon (GtC)
Δ[CO3 2-] (µmol kg-1)
d
Atmospheric pCO2 (ppm)
EDML
Byrd
MIS 4
MIS 5a
Age (ka)

Figure 3

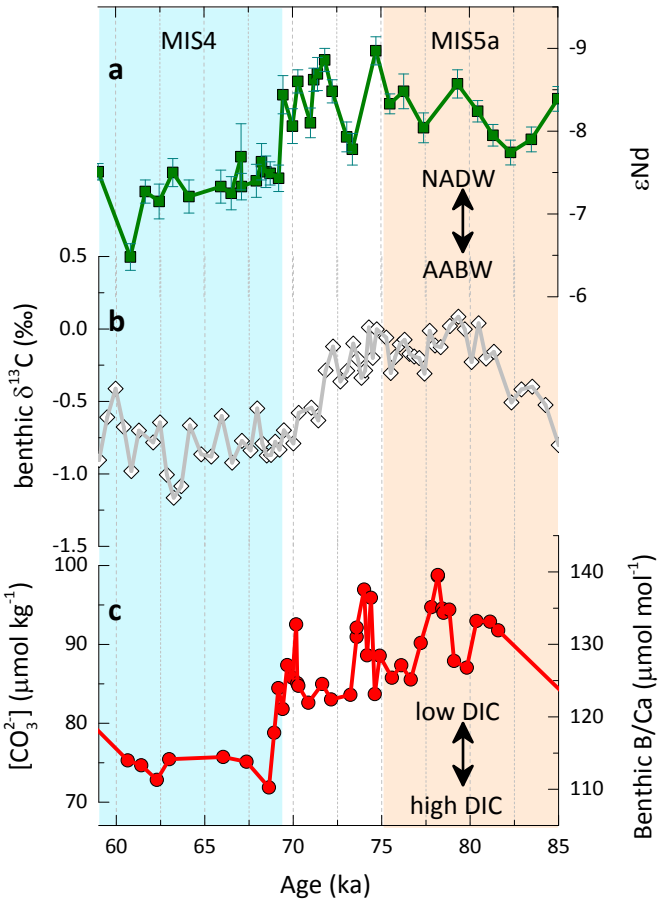
MIS4
MIS5a
a
b
c
NADW
AABW
low DIC
high DIC
εNd
benthic δ13C (‰)
[CO32-] (µmol kg-1)
Benthic B/Ca (µmol mol-1)
Age (ka)
-9
-8
-7
-6
0.5
0.0
-0.5
-1.0
-1.5
100
90
80
70
140
130
120
110
60
65
70
75
80
85

Figure 4

Sequestration of carbon in the deep Atlantic during the last glaciation

J. Yu[1]*, L. Menviel[2,3], Z.D. Jin[4], D.J.R. Thornalley[5], S. Barker[6], G. Marino[1], E.J. Rohling[1,7], Y. Cai[4], F. Zhang[4], X. Wang[8], Y. Dai[1], P. Chen[1,9], W.S. Broecker[10]

1. Deep water [CO_3^{2-}], ALK, and DIC

We use the Global Ocean Data Analysis Project (GLODAP) dataset[1] and model outputs from LOVECLIM and the UVic ESCM[2-4] to explore the relationship between deep-water [CO_3^{2-}], ALK and DIC. For the GLODAP dataset, the anthropogenic CO_2 contribution was subtracted from the measured DIC to obtain the pre-industrial (PI) values. Deep-water [CO_3^{2-}] was calculated using CO2sys.xls[5] with K_1 and K_2 according to Mehrbach et al.[6] and K_{SO4} according to Dickson[7]. Seawater total boron concentration was calculated from the recent B-S relationship by *Lee et al.*[8].

Traditionally, seawater [CO_3^{2-}] is approximated by the following relationship[9]

$$[CO_3^{2-}] \approx ALK - DIC \qquad (a)$$

This approximation provides a handy but qualitative way to describe the relationship between changes in [CO_3^{2-}], ALK and DIC. However, for given ALK and [CO_3^{2-}], this relationship systematically overestimates DIC (absolute values) and underestimates the change in DIC by ~22% (a shallower slope than 1) (Supplementary Fig. 1). We find that deep water [CO_3^{2-}] is

strongly correlated with ALK-DIC in the GLODAP dataset, and the relationship may be described by:

$$[CO_3^{2-}] = k \times (ALK - DIC) + b \qquad (b)$$

where k = 0.59±0.01 and b = 16±1 μmol/kg (1σ). If the changes (Δ) of variables are of interest, Equation (b) can be used to derive Equation (1) presented in the main text:

$$\Delta_{[CO_3^{2-}]} = k \times (\Delta_{ALK} - \Delta_{DIC}) \qquad (1)$$

From Equation (1), we derive $\Delta_{DIC} = \Delta_{ALK} - \Delta_{[CO_3^{2-}]}/0.59$. If $\Delta_{ALK} = 0$, then $\Delta_{DIC}/\Delta_{[CO_3^{2-}]} = -1/k = -1/0.59$ (the blue line trend in Fig. 1c). Note that this slope cannot be directly compared with the regression of DIC-$[CO_3^{2-}]$ (the red line in Fig. 1c), because the -1/k trend (blue line in Fig. 1c) assumes no change in ALK while the regression of DIC-$[CO_3^{2-}]$ implicitly includes the spatial ALK changes. In Fig. 1c, the -1/0.59 slope (i.e., k = 0.59 and $\Delta_{ALK} = 0$ in Equation (1); blue line) is shallower than the trend (red line) defined by data, because the regression of the data (red line) includes ~40 μmol/kg ALK increase from the deep North to South Atlantic. In the preindustrial deep Atlantic, $\Delta_{ALK} = -1.02 \times \Delta_{[CO_3^{2-}]}$ (Fig. 1d). Thus, when ALK changes are included, $\Delta_{DIC} = -1.02 \times \Delta_{[CO_3^{2-}]} - \Delta_{[CO_3^{2-}]}/0.59 = (-1.02 - 1.69) \times \Delta_{[CO_3^{2-}]} = -2.71 \times \Delta_{[CO_3^{2-}]}$. The -2.71 slope matches well with the best fit of observed DIC to $[CO_3^{2-}]$ slope of -1/0.37 = -2.70 (Fig. 1c). This supports that the relationship between $[CO_3^{2-}]$ and DIC adhere to a k value of 0.59, when the ALK change is included in the calculation of DIC for the preindustrial deep Atlantic. The feasibility of using a k value of 0.59 is straightforwardly demonstrated by Supplementary Fig. 1b which shows the close match between measured DIC and predicted DIC based on Equation (1) with a k value of 0.59 taking account of ALK changes.

Due to numerous equations and dissociation constants involved in the seawater carbonate system[10], it is difficult to predict k using theoretical calculations. To check the applicability of the empirically derived k for the glacial oceans, we investigate the relationship between [CO_3^{2-}] and ALK-DIC in two numerical models LOVECLIM and UVic ESCM[2-4] (see Section 8). As shown by Supplementary Fig. 2, control experiments performed with these models give a range of k from 0.55 to 0.59 during the PI and the LGM, close to the value derived based on the GLODAP dataset (Supplementary Fig. 1). In addition, experiments in which NADW was weakened or shutdown display a k range of 0.53 to 0.55 (Supplementary Fig. 2e-h). Altogether, numerical models give a k range of 0.525-0.59, with a mean value of 0.55.

2. Core materials and analytical methods

Our new deep water [CO_3^{2-}] reconstructions are based on B/Ca measurements of the epibenthic (a habitat above the sediment-water interface) foraminiferal species *Cibicidoides wuellerstorfi* from 7 cores (Supplementary Table 1). About 10 cc of sediments were disaggregated in de-ionized water and wet sieved through 63 μm sieves for each sample (1-2 cm depth interval). All *C. wuellerstorfi*, ranging from ~10 to 20 shells in each sample, were picked for all samples from the 250-500 μm size fraction. The shells were then double checked under a microscope before crushing with due attention to use shells of consistent morphology for B/Ca analyses throughout the core[11]. On average, the starting material for each sample has ~8-12 shells, equivalent to ~300 to 600 μg of carbonate. Except for tests from cores RC13-228 and EW9209-2JPC, which were cleaned following the "Cd-cleaning" protocol[12], shells from other cores were cleaned by the “Mg-cleaning” method[13,14]. Foraminiferal B/Ca was measured on ICP-MS using the established procedure[15]. The analytical error in B/Ca is ~±2.5% or ~±3 μmol/mol

(1σ), based on repeated measurements of an internal standard (B/Ca = 150 μmol/mol). Foraminiferal B/Ca shows no correlation with Mn/Ca, Al/Ca or Fe/Ca (not shown), indicating that B/Ca is not biased by contamination from diagenetic coatings or silicates.

We have increased the resolution of the B/Ca record during MIS 4 in core RC16-59. Core RC16-59 is somewhat special in that shells from this core appeared crystal clean after de-ionized water and methanol rinses, but turned yellow after the oxidizing step as documented in ref. [16]. The reasons for this phenomenon remain unknown, but we speculate that the yellow color may be caused by some coating (organic or other types?). To explore possible effects from these coatings, we cleaned 9 additional samples from RC16-59. Consistent with ref. [16], shells indeed turned yellow during the oxidizing step. B/Ca ratios of the new samples confirm the pattern defined by the published data[16].

To further explore the effect of coatings on B/Ca and to double check the large B/Ca amplitude between MIS 5a and 4 revealed by RC16-59 (Fig. 2, 3), we worked on a nearby core EW9209-2JPC, from the Ceara Rise. As expected, tests from core depths >250 cm turned yellow during the oxidizing step (shells from <20 cm remained white/clean). These shells were then subjected to a reductive cleaning step[17], after which all shells appeared crystal clean under a microscope. B/Ca ratios from core EW9209-2JPC are similar to those from core RC16-59 (Fig. 2b). Therefore, we believe that B/Ca ratios are not biased by the coating at our sites. The new B/Ca results reproduce the large $B/Ca_{MIS5a-4}$ amplitude shown by RC16-59 (Supplementary Fig. 7).

Benthic foraminiferal $\delta^{18}O$ and $\delta^{13}C$ measurements were made for *C. wuellerstorfi* and *Uvigerina* spp. at the Earth Environment Institute, Chinese Academy of Science and the Research School of Earth Sciences at the Australian National University. No analytical offset

between the two labs is observed, based on aliquots of samples from cores RC16-59 (ref. [16]) and MD01-2446. *C. wuellerstorfi* $\delta^{18}O$ and $\delta^{13}C$ from core MD95-2039 were measured at Cardiff University. When applicable, a constant -0.64‰ has been applied to $\delta^{18}O$ in *Uvigerina* spp. to convert to *C. wuellerstorfi* equivalent values. The average analytical error is ~0.08‰ in both $\delta^{18}O$ and $\delta^{13}C$.

The $\%CaCO_3$ data shown in Fig 2 are from this study for MD95-2039, ref. [18] for RC16-59, ref. [19] for GeoB1117, ref. [20] for RC13-228, ref. [21] for RC13-229, and ref. [22] for TNO57-21.

3. Conversion of benthic B/Ca into deep water $[CO_3^{2-}]$

Measurements of core-top samples from the global deep ocean[23] show that *C. wuellerstorfi* B/Ca may be empirically calibrated against the deep water carbonate saturation state ($\Delta[CO_3^{2-}]$) by[23-27]:

$$B/Ca = 1.14 \times \Delta[CO_3^{2-}] + 177, \quad R^2 = 0.81 \qquad (c)$$

where $\Delta[CO_3^{2-}] = [CO_3^{2-}] - [CO_3^{2-}]_{saturation}$. Thus,

$$B/Ca = 1.14 \times ([CO_3^{2-}] - [CO_3^{2-}]_{saturation}) + 177 \qquad (d)$$

Here, term $[CO_3^{2-}]_{saturation}$ is mainly controlled by pressure (water depth)[10] and remains roughly stable in the deep sea on glacial-interglacial timescales[28] due to the relatively small effect from sea level change (<~120 m)[29]. Assuming that the core-top $[CO_3^{2-}]$ equals the preindustrial (PI) value, then

$$\Delta B/Ca_{downcore\text{-}coretop} = 1.14 \times ([CO_3^{2-}]_{downcore} - [CO_3^{2-}]_{PI}) \qquad (e)$$

where $[CO_3^{2-}]_{PI}$ is estimated using the GLODAP dataset[1] (Supplementary Table 1), and $\Delta B/Ca_{downcore\text{-}coretop}$ represents the deviation of B/Ca of down-core samples from the core-top value. Therefore,

$$[CO_3^{2-}]_{downcore} = [CO_3^{2-}]_{PI} + \Delta B/Ca_{downcore\text{-}coretop}/1.14 \qquad (f)$$

We quote an uncertainty of ±5 μmol/kg (1σ) in $[CO_3^{2-}]$, based on the error derived from the global core-top calibration samples[23,25]. Deep water $[CO_3^{2-}]$ reconstructions for cores GeoB 1115/1117/1118 and RC16-59 are from refs. [16,26].

Equation (f) only requires use of the slope (1.14 μmol/mol per μmol/kg) from the core-top calibration, since the main interest lies in the pattern and amplitude of $[CO_3^{2-}]$ within individual cores. Because core-top samples do not always plot directly on the calibration line, inclusion of the intercept in the calculation would sometimes result in an offset between the core-top (<~5 ka) and PI values. Although within the reconstruction uncertainty, such an offset may unnecessarily complicate the comparison of downcore records between cores. We suggest that by matching the core-top values to the PI values, we "normalize" all downcore reconstructions based on the PI condition, a reference against which many paleoceanographic records are considered. This may help to minimize any systematic error downcore, and thus facilitate core-to-core comparisons.

Supplementary Fig. 3 shows core-top $[CO_3^{2-}]$ calculated using both slope and intercept from Equation (c). The reconstructions derived from benthic foraminiferal B/Ca compare well, within reconstruction uncertainty, with the deep water $[CO_3^{2-}]$ estimated using nearby hydrographic sites compiled by GLODAP[1].

Our main interest here is to investigate the changes in B/Ca and $[CO_3^{2-}]$ between MIS 5a and 4. We have used the following method to calculate the uncertainties associated with B/Ca

and $[CO_3^{2-}]$ shown in Fig. 3a and Supplementary Table 4. For each time period, 1sd represents the one standard deviation of all B/Ca and B/Ca-derived $[CO_3^{2-}]$ values. When calculating the difference between MIS 5a and 4, we also include the uncertainty (±0.04 μmol/mol per μmol/kg, 1σ) associated with the B/Ca-$\Delta[CO_3^{2-}]$ slope (1.14 μmol/mol per μmol/kg)[23]. From Equation (f), one may derive:

$$\Delta_{[CO_3^{2-}]_{MIS5a-4}} = \Delta B/Ca_{MIS5a-4} / (1.14 \pm 0.04) \quad \text{(g)}$$

The relative and absolute errors in $\Delta_{[CO_3^{2-}]_{MIS5a-4}}$ are calculated, respectively, by

$$\%\text{err}\Delta_{[CO_3^{2-}]_{MIS5a-4}} = \sqrt{(\%\Delta B/Ca_{err})^2 + (\%slope_{err})^2} \quad \text{(h)}$$

and

$$\text{err}\Delta_{[CO_3^{2-}]_{MIS5a-4}} = \Delta_{[CO_3^{2-}]_{MIS5a-4}} \times \%\text{err}\Delta_{[CO_3^{2-}]_{MIS5a-4}} \quad \text{(i)}$$

4. Age models

We construct age models for sediment cores MD95-2039, MD01-2446, EW9209-2JPC, RC16-59, RC13-228, and RC13-229 based on comparisons of benthic $\delta^{18}O$ with the LR04 stack curve[30] (Supplementary Table 2). By using one target curve for tuning, we minimize potential relative age offsets between cores. Age models are from ref. [31] for TNO57-21 and ref. [19] for GeoB cores. Supplementary Fig. 4 shows benthic $\delta^{18}O$ in each core relative to the LR04 curve.

Cores RC13-228 and RC13-229 are located close to the Namibia upwelling region. Comparison of benthic $\delta^{13}C$ in these cores with $\delta^{13}C$ data for cores located at similar water depths but outside the upwelling region[32] suggests that deep water chemistry at these sites from

MIS 5 to 4 is not significantly affected by organic matter regeneration associated with surface productivity due to coastal upwelling (Supplementary Fig. 5, 6). Therefore, signals recorded by benthic shells from these cores are not biased by local effects, but likely reflect the open ocean conditions.

5. Deep Atlantic carbonate ion and probabilistic assessment of uncertainties

First, we spliced the B/Ca-based reconstructions of the deep ocean [CO_3^{2-}] variability from 10 deep Atlantic Ocean sediment cores (Fig. 1a, 2, 3b) which are placed on the LR04 timescale[30] (Supplementary Fig. 4). Second, we used a Monte Carlo-style approach to probabilistically evaluate the uncertainties associated both with the chronology (i.e., the synchronization error to the LR04 benthic stack) and with the B/Ca measurements and calibration of the deep Atlantic [CO_3^{2-}] composite record (see above)[23,25]. Specifically, all individual data points were separately and randomly sampled 5,000 times within their chronological (±2 ka, 1σ) and [CO_3^{2-}] (±5 μmol/kg, 1σ) uncertainties and each of these iterations was then linearly interpolated. At each time step the probability distribution of the 5,000 iterations was assessed and the 68% (16^{th}-84^{th} percentile) and 95% (2.5^{th}-97.5^{th} percentile) probability intervals of the data were determined. The probability maximum shown in Fig. 3c is the modal value at each time step and the shaded envelope represents its standard error at the 95% probability level. For details on this approach, see e.g., [29,33].

6. Deep Atlantic carbon budget calculation

We take a simple approach to calculate the first order carbon budget change in the deep Atlantic Ocean from MIS 5a to MIS 4.

First, we consider the "deep Atlantic Ocean" as the basin at >3 km water depth. Volume and mass of the waters in the deep Atlantic Ocean are 9.8×10^{16} m^3 and 10.1×10^{19} kg, respectively[34]. The values are assumed constant in the past.

Second, the average decrease (~28 μmol/mol) in benthic B/Ca is translated into ~25 μmol/kg reduction in deep water [CO_3^{2-}], based on a B/Ca-[CO_3^{2-}] sensitivity of 1.14 μmol/mol per μmol/kg[23]. In view of the wide geographic distribution of the studied cores, we assume the ~25 μmol/kg reduction from MIS 5a to MIS 4 to be representative of the entire deep Atlantic Ocean.

Third, as there is strong evidence that the observed [CO_3^{2-}] reduction was not caused by an ALK decrease (see main text), we assume no change in ALK; i.e., $\Delta_{ALK} = 0$ μmol/kg. In this case and using k of 0.59 based on the GLODAP dataset (Supplementary Fig. 1), Equation (1) becomes $\Delta_{[CO_3^{2-}]} = -0.59 \times \Delta_{DIC}$, or $\Delta_{DIC} = -\Delta_{[CO_3^{2-}]}/0.59$. From MIS 5a to MIS 4, $\Delta_{DIC} = -(-25$ μmol/kg)/0.59 = 42 μmol/kg.

Fourth, the total C change is $\Delta_{DIC} \times 10.1 \times 10^{19}$ kg = 427×10^{19} μmol = 5121×10^{13} g C = 51.2 Pg C. Using k values (range: 0.525-0.59; mean: 0.55) independently derived from biogeochemical models (Supplementary Fig. 2) would yield a carbon storage change of ~55 Gt (range: 51-58 Gt).

The uncertainties are propagated through the same equations based on errors associated with the deep water [CO_3^{2-}] reconstructions.

7. Carbonate compensation and deep water [CO_3^{2-}]

Previous modeling studies[35-37] suggest that, after a perturbation, the *global mean* deep ocean [CO_3^{2-}] should return to the initial value on a timescale of ~5,000-7,000 years via a process called "carbonate compensation"[35], to maintain the *global* ALK balance between inputs and outputs. The underlying assumptions to predict deep water [CO_3^{2-}] changes based on carbonate compensation include that, over the time scale of consideration, (i) ALK inputs from rivers and hydrothermal vents remain stable; (ii) the magnitude and spatial pattern of $CaCO_3$ export from the surface is constant; (iii) pelagic (shelf) $CaCO_3$ burial remains unchanged; (iv) $CaCO_3$ dissolution in the water column and pore water is minimal or stays the same through time[35,38]; and (v) the influence of ocean circulation remains similar[35,39]. Under such conditions, deep-sea $CaCO_3$ burial, largely controlled by deep water [CO_3^{2-}], determines the variations of the ALK removal from the ocean. Carbonate compensation serves as a negative feedback between deep water [CO_3^{2-}] and the oceanic ALK inventory via $CaCO_3$ preservation on the sea floor: a decrease in deep water [CO_3^{2-}] enhances deep-sea $CaCO_3$ dissolution, which raises the whole ocean ALK and thereby brings deep water [CO_3^{2-}] back to a steady state where ALK input is matched by ALK output, and *vice versa*. With the assumptions above, the global mean deep ocean [CO_3^{2-}] at steady states is expected to stay constant so that the ALK output matches the ALK input.

However, it is important to note that any variation in the assumptions associated with carbonate compensation would result in different responses in the deep ocean [CO_3^{2-}]. For example, everything else being equal, a decrease in the global weathering would cause a permanent decrease in the global mean deep ocean [CO_3^{2-}] at a new steady state (Supplementary Fig. 14a). The reduced weathering flux of ALK may be caused by cold and dry conditions during

glacial times[35], although we acknowledge that further work is needed to estimate the opposing effects, such as exposure of carbonates on shelves, which tend to raise the weathering rate during glacials[40]. Another example to cause a long-term drop in the deep ocean [CO_3^{2-}] is to increase the surface $CaCO_3$ export[41] (Supplementary Fig. 14b). In both cases, although not returning to the initial value, deep-sea [CO_3^{2-}] is still influenced by carbonate compensation, and the global ALK input and output are balanced at the new steady state. Supplementary Fig. 14 demonstrates potential complicating factors affecting the deep water [CO_3^{2-}] changes associated with carbonate compensation.

We propose two scenarios to explain the sustained low [CO_3^{2-}] in the deep Atlantic during MIS 4 (Fig. 2). Scenario 1 invokes different carbonate chemistry between Atlantic and Pacific Oceans to explain a stability of the global mean deep-water [CO_3^{2-}] at steady state. This considers that (i) deep Atlantic [CO_3^{2-}] does not represent the global mean deep ocean [CO_3^{2-}], (ii) the deep Pacific possibly had a higher steady-state [CO_3^{2-}] during MIS 4 than during MIS 5a, as suggested by previous records (e.g., ref. [25,42]), and (iii) the global mean deep-sea [CO_3^{2-}] might have remained roughly stable at steady state, as suggested by previous modeling studies[36,39]. As illustrated by Fig. 7 in Boyle (1988)[36], the deep Atlantic [CO_3^{2-}] can be maintained at a lower value during the "glacial" than during the "interglacial" for an extended period of time. The global mean deep-sea [CO_3^{2-}] remains stable at steady state, because the deep Pacific had a higher [CO_3^{2-}] during the "glacial". In his model, Boyle (1988) fully considered the carbonate compensation effect. Our reconstructions for MIS 4 in the deep Atlantic is consistent with Boyle's prediction, and does not contradict the carbonate compensation theory. Focusing on the Holocene and the LGM, Emerson and Archer (1992)'s work[39] is also consistent with our reconstructions. They argued that the calcite saturation horizon was permanently shallower

(lower glacial deep-water [CO_3^{2-}]) in the deep Atlantic during the LGM than today, while the opposite is true for the deep Indo-Pacific Oceans (higher glacial [CO_3^{2-}]) (Fig. 4 in ref. [39]). This results in a similar global mean deep water [CO_3^{2-}] between the Holocene and the LGM. If one considers the transition from Holocene to the LGM (the change back in time), the variations of the deep ocean carbonate chemistry suggested by Emerson and Archer[39] are analogous to what we see for the transition from MIS 5a to MIS 4 (the evolution through time).

Scenario 2 invokes a decline in the weathering rate coupled with an AMOC weakening for the sustained low deep Atlantic [CO_3^{2-}] during MIS 4, as demonstrated by our numerical simulations (Supplementary Fig. 15-19; see Section 8). In both long experiments ("weakened NADW" and "NADW off") performed with the UVic ESCM, deep Atlantic [CO_3^{2-}] can decrease and stay below its initial value for about 9,000 years. As the alkalinity budget is kept constant in the model and as the carbonate burial is reduced, so is the alkalinity input from the river (Section 8.1). Our approach here is to use the modelling experiments to understand possible mechanisms (at least in theory) responsible for the prolonged reduced deep Atlantic [CO_3^{2-}] observed in our marine sediment cores. It seems that reduced river influx of alkalinity during the MIS 5a-MIS 4 transition could explain this long negative [CO_3^{2-}] anomaly. Considering the reduced influx of ALK, the global mean deep-water [CO_3^{2-}] should stay at lower values. In other words, the sustained low deep water [CO_3^{2-}] during MIS 4 does not contradict the carbonate compensation theory.

At present, insufficient data are available to confidently distinguish the feasibility of the two scenarios for the sustained low [CO_3^{2-}] shown by our records (Fig. 2, 3). To unveil the ultimate reason for the sustained low [CO_3^{2-}], detailed records from the deep Pacific Ocean have to be considered along with the requirement for improved knowledge on weathering during that

time period. However, the two possibilities are not mutually exclusive and are both consistent with the carbonate compensation theory.

Given the exposure of shelves that tends to raise the carbonate weathering rate[40], we surmise that weathering rate may have remained roughly unchanged on the timescale of consideration here. If correct, then Scenario 1 would be favored. Because of increased carbon sequestration in the glacial ocean, a relatively stable global mean deep-sea [CO_3^{2-}] would suggest an increased ALK inventory. Taking this global ALK inventory increase into account, our estimate of carbon storage change in the deep Atlantic would be increased during MIS 4.

8. Idealized numerical experiments

In two Earth system models of intermediate complexity (UVic ESCM and LOVECLIM), the NADW formation was halved or shut down to investigate influences of AMOC changes on the deep Atlantic [CO_3^{2-}]. The UVic ESCM includes an ocean general circulation model of horizontal resolution 3.6°x1.8° with 19 vertical layers[2], fully coupled to a marine carbon cycle and a sediment model[43,44]. The UVic ESCM atmospheric component is an energy-moisture balance model. LOVECLIM includes an ocean general circulation model of horizontal resolution 3°x3° with 20 vertical layers, coupled to a marine carbon cycle[45]. The atmospheric component of LOVECLIM is a quasi-geostrophic T21 model. Control run experiments were performed with both models and for both pre-industrial and LGM conditions[46]. North Atlantic Deep Water formation was halved or shut down, under constant pre-industrial boundary conditions, to investigate influences of AMOC changes on deep Atlantic [CO_3^{2-}] and term k values (Section 1; Supplementary Fig. 2).

8.1. Long (9,000-yr) simulations performed with the UVic ESCM

Our results from two long simulations detailed below suggest that it is possible to achieve low [CO_3^{2-}] over a duration of up to ~10 kyr. Both "halved" and "shutdown" NADW numerical experiments indicate that AMOC changes significantly impact deep Atlantic [CO_3^{2-}]. The modeled deep Atlantic [CO_3^{2-}] reductions are consistent with our estimates based on benthic B/Ca and other qualitative proxies (e.g., %$CaCO_3$) (Fig. 2-4).

Experiment with 50% reduction in NADW

In this experiment, NADW is halved by adding 0.1 Sv freshwater into the North Atlantic for 9,000 years under constant pre-industrial boundary conditions. A 50% reduction of NADW formation leads to a deep (>3 km) [CO_3^{2-}] decrease in the North and Equatorial Atlantic on the order of 30 μmol/kg (Supplementary Fig. 15). In the deep South Atlantic, the decrease amounts to ~22 μmol/kg. This is due to a ~60 μmol/kg DIC increase in the deep Atlantic associated with reduced ventilation and increased accumulation of remineralized carbon. On the other hand, deep Atlantic ALK increases by ~15 μmol/kg in the deep Atlantic. As there are no significant changes in the other water masses, DIC also increases in the deep Pacific, resulting in ~8 μmol/kg decrease in [CO_3^{2-}] in the deep Western Equatorial Pacific (Supplementary Fig. 15).

The globally reduced deep [CO_3^{2-}] contributes to ~25% drop in the global $CaCO_3$ burial (Supplementary Fig. 16). Changes in ocean stratification brought about by the reduced NADW leads to a 12% decrease in global export production of $CaCO_3$ (Supplementary Fig. 17), which helps to lower $CaCO_3$ burial. In this version of the model, sediment burial is compensated for by riverine influxes of ALK and DIC for mass conservation. As a result, the riverine ALK (and

DIC) input is also lowered (by up to 35%) so that the global mean ALK is constant at 2424.43 μmol/kg throughout the experiment. As mentioned above (Section 7), the reduced weathering flux of ALK may be caused by cold and dry conditions during glacial times[35].

As can be seen in the Hovmoeller diagram (Supplementary Fig. 18), deep water [CO_3^{2-}] rapidly decreases at depth, whereas [CO_3^{2-}] increases above 1500 m. The fact that both paleoproxy records and modeling experiments show a mean deep [CO_3^{2-}] decrease support the idea of reduced NADW at MIS 5a-4 transition, which helps isolating the deep ocean from the surface. The lack of a return to the original global mean deep [CO_3^{2-}] on a timescale greater than 5,000 years is caused by reduced riverine influx of ALK to the ocean (Supplementary Fig. 14). In other words, when the changes in riverine input are taken into account, a permanent reduction in the deep ocean [CO_3^{2-}] is not inconsistent with carbonate compensation.

Experiment with NADW cessation

In this experiment, NADW is turned off by adding 0.15 Sv freshwater into the North Atlantic for 3,000 years under constant pre-industrial boundary conditions. As the UVic ESCM is bi-stable, once NADW is off it does not restart on its own. The experiment was thus integrated until year 9,000 without any freshwater addition between years 3,000 and 9,000. A cessation of NADW formation leads to a deep (>3 km) [CO_3^{2-}] decrease in the North and Equatorial Atlantic by ~20-40 μmol/kg (Supplementary Fig. 19). In the deep South Atlantic, the decrease amounts to ~22 μmol/kg. DIC increases by up to 180 μmol/kg in the deep North Atlantic (yr 4,000) due to the reduced ventilation and increased accumulation of remineralized carbon in the deep North Atlantic. Deep Atlantic ALK increases by up to 120 μmol/kg.

A cessation of NADW formation with a closed Bering Strait leads to the formation of North Pacific Deep Water (NPDW) in the UVic ESCM[47] (Supplementary Fig. 19). NPDW ventilates the intermediate and deep North Pacific, thus decreasing the DIC content and leading to a deep [CO_3^{2-}] rise in the Pacific. In addition, as the freshwater input in the North Atlantic is stopped at year 3,000 and NPDW leads to a slight sea surface salinity increase, AABW formation strengthens at year 3,000. The enhanced AABW ventilates the deep Ocean, reducing DIC and raising [CO_3^{2-}] of deep waters.

The globally reduced deep [CO_3^{2-}] contributes to a global $CaCO_3$ burial decrease of about 14% (Supplementary Fig. 16). As sediment burial is compensated for by riverine influx of ALK and DIC for mass conservation, the riverine ALK input is also lowered (by ~30-40% during years ~1,000-4,000) so that the global mean ALK is constant throughout the experiment (2424.43 μmol/kg). Changes in ocean stratification brought about by NADW cessation leads to a 15% decrease in global export production and in $CaCO_3$ export at year 1,500. However, as NPDW and AABW strengthen, $CaCO_3$ export returns to its initial global mean by year 6,000. The $CaCO_3$ export pattern is different from its initial state as shown in Supplementary Fig. 20.

Supplementary Fig. 21 shows that deep [CO_3^{2-}] rapidly decreases at depth, whereas above 1500 m [CO_3^{2-}] increases. Maximum anomalies are obtained at year ~4,000. Enhanced formation of NPDW and AABW reverses the trends with deep [CO_3^{2-}] increasing below 1500 m and [CO_3^{2-}] decreasing above 1500 m.

Summary

Our modeling results show that, when NADW is weakened or shutdown, deep water [CO_3^{2-}] in the deep Atlantic can stay low for >~8,000 years, consistent with the results from

proxies (Fig. 2). Our data (Fig. 2) and modeling results (Supplementary Fig. 15-21) suggest that multiple factors should be considered when using deep water [CO_3^{2-}] to investigate influences from deep-sea carbonate compensation. Note that the ALK influx from rivers is left floating (lower fluxes for both "weakened" and "off" NADW experiments) to keep the global ALK at a constant value in UVic ESCM. If the riverine ALK flux remained constant during the MIS 5a to MIS 4 transition, then global ALK would most likely increase, resulting in a smaller [CO_3^{2-}] decline in the deep Atlantic, in response to the AMOC change. This increase in global ALK inventory would raise the carbon storage estimate based on Equation (1), for a given reconstructed change in deep Atlantic [CO_3^{2-}].

8.2. Short (1,000-yr) simulation using LOVECLIM

We ran a short simulation using LOVECLIM. From a pre-industrial control run which is described in detail elsewhere[2,3,45,48], the NADW formation was weakened by adding 0.06 Sv of freshwater into the northern North Atlantic for 1,000 years. The NADW weakening, from 25 to 12 Sv, is associated with a shoaling of the NADW-AABW boundary to ~2600 m in LOVECLIM (Supplementary Fig. 22). In comparison, the NADW-AABW boundary shoals to ~2200 m at year 1,000 in the UVic ESCM. In both models, weaker ventilation of the deep Atlantic Ocean leads to a DIC increase from 26 to 41 μmol/kg, and an alkalinity rise from 13 to 15 μmol/kg below 3300 m[46]. This results in a [CO_3^{2-}] reduction in the Atlantic basin below ~1500 m (Supplementary Fig. 22), in relative agreement with the [CO_3^{2-}] anomalies estimated from marine sediment cores (Fig. 2). Deep water oxygen concentrations stay above the anoxic level (>~20 μmol/kg) in both the Atlantic and Pacific in LOVECLIM and UVic ESCM models (Supplementary Fig. 23).

8.3. Preformed and remineralized nutrients and DIC

Upon reaching the North Atlantic Ocean, surface waters are depleted in nutrients, thus the preformed nutrient content in NADW is low. On the other hand, nutrient utilization is low in the Southern Ocean, thus AABW has a relatively high preformed nutrient content. This contrast in preformed nutrient content is marked in the UVic ESCM, but weaker in LOVECLIM.

When NADW weakens, the deep Atlantic is less ventilated, thus leading to an increase in remineralized nutrients and carbon. The global inventory of preformed phosphate over total phosphate thus decreases in all experiments during the first ~1,500 years (Supplementary Fig. 24) as the proportion of remineralized phosphates increases. As shown in Supplementary Fig. 19, AABW strengthens at ~year 3,000 in the UVic ESCM experiment with NADW off, which drives a strong increase in the global preformed phosphate content. Similarly, in the 50% NADW weakening experiment performed with the UVic ESCM, it is a small increase in AABW that is driving the moderate increase in preformed phosphates at ~ year 1,500. However, the UVic ESCM does not simulate an increase in export production in the Southern Ocean following a NADW weakening, which could lead to an overestimate of the preformed phosphate increase in southern-sourced waters.

The DIC response to changes in oceanic circulation can be separated into different contributions from the soft-tissue pump (C_{soft}), the carbonate pump (C_{carb}) and the gas-exchange pump (C_{gasx}) (e.g. [49]):

$$\Delta DIC = \Delta C_{soft} + \Delta C_{carb} + \Delta C_{gasx} \qquad (j)$$

Changes in the soft-tissue pump are related to the remineralization of organic carbon:

$$\Delta C_{soft} = C/P \times \Delta PO_4^{Rem} \quad (k)$$

$$\Delta PO_4^{Rem} = \Delta PO_4^{Tot} - \Delta PO_4^{Pref} = \Delta AOU \times P/O_2 \quad (l)$$

$$AOU = O_2^{sat} - O_2 \quad (m)$$

where Δ means changes of parameters; C/P and P/O_2 represent the Redfield ratios of carbon-to-phosphate and phosphate-to-oxygen, respectively; PO_4^{Tot}, PO_4^{Pref}, and PO_4^{Rem} represent total, preformed, and remineralized phosphate concentrations, respectively; AOU is the Apparent Oxygen Utilization; and O_2^{sat} is the saturated dissolved oxygen content based on temperature and salinity.

As shown previously (e.g., [50]), most of the DIC changes occurring in the Atlantic basin during a weakening/shutdown of NADW can be explained by changes in C_{soft}. Supplementary Fig. 25 shows that C_{soft} increases in the deep Atlantic while decreases in the intermediate North Atlantic, when NADW is weakened in LOVECLIM and the UVic ESCM. This mostly represents the accumulation of remineralized carbon in the deep ocean due to weaker ventilation.

Supplementary Figures:

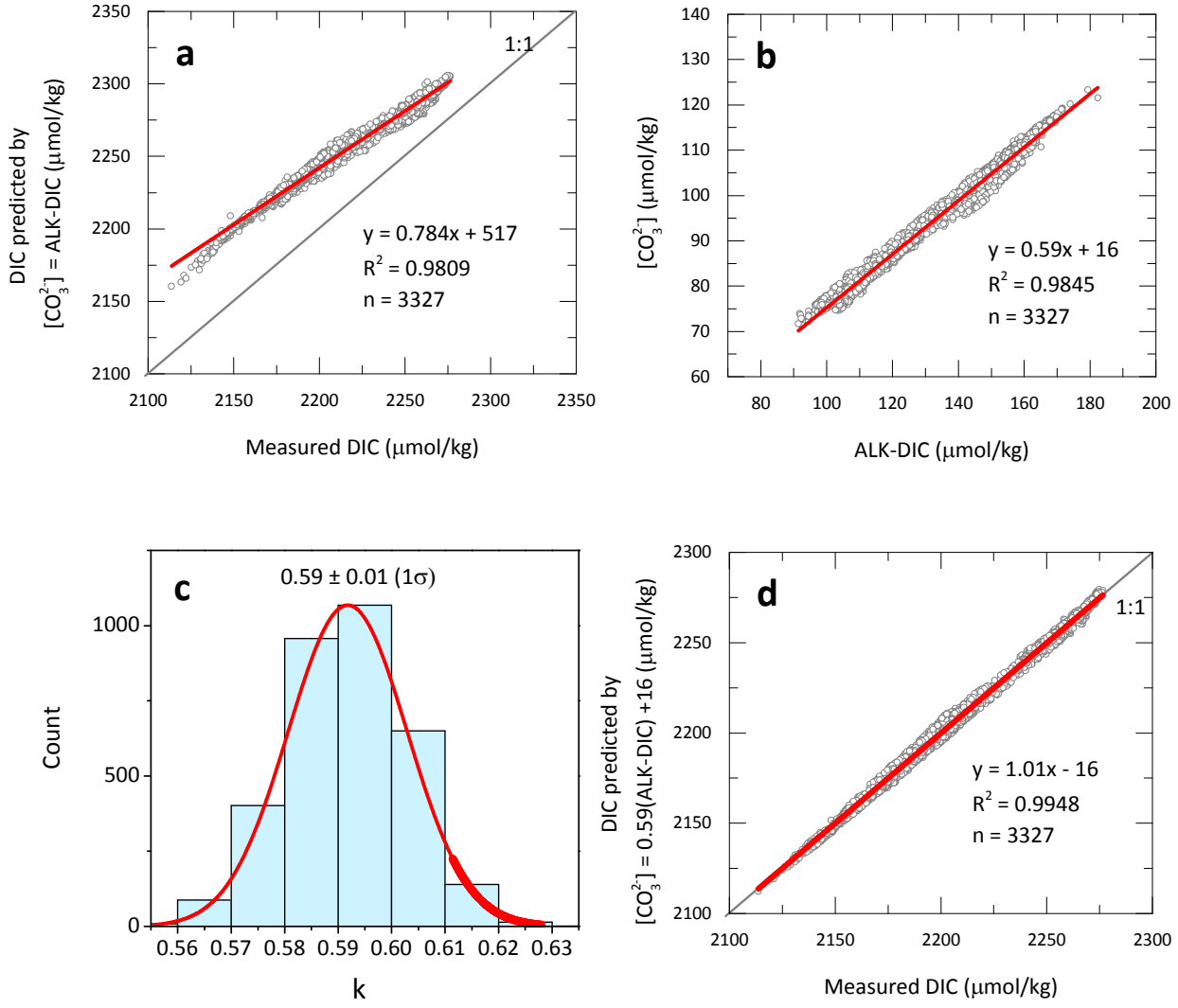

Supplementary Figure 1 | Relationship between $[CO_3^{2-}]$ and ALK-DIC in the deep Atlantic (>2.5 km water depth) compiled by the GLODAP dataset[1]. a, DIC predicted by $[CO_3^{2-}]$ = ALK - DIC. **b,** $[CO_3^{2-}]$ vs. ALK - DIC. **c**, Variation of term k, defined as k = ($[CO_3^{2-}]$ - 16)/(ALK − DIC). **d**, DIC predicted by $[CO_3^{2-}]$= 0.59 × (ALK − DIC) + 16.

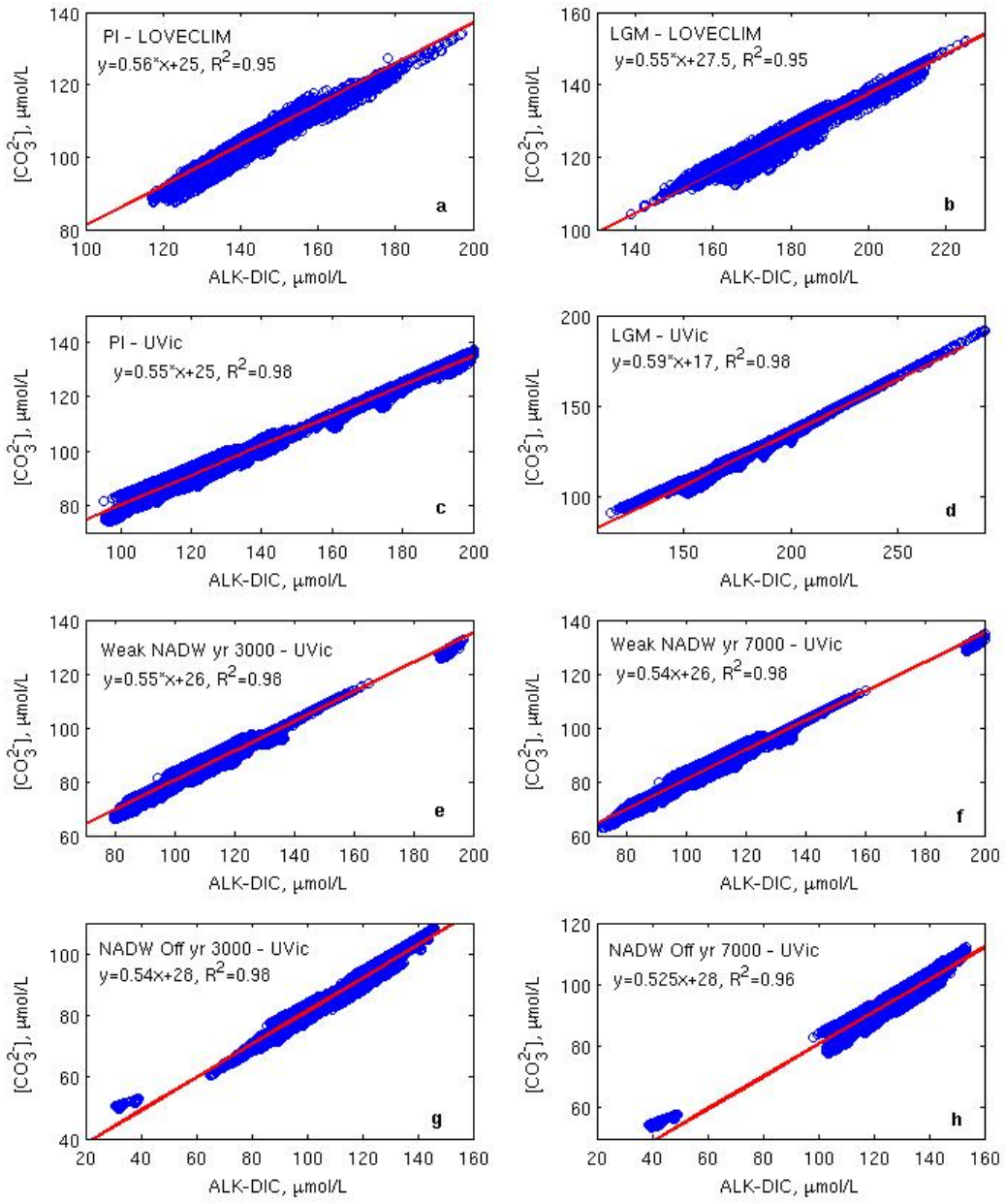

Supplementary Figure 2 | Relationship between deep-water (>2.5 km) [CO_3^{2-}] and ALK-DIC from models. Pre-industrial (PI) data from (**a**) LOVECLIM and (**c**) UVic ESCM. LGM data from (**b**) LOVECLIM and (**d**) UVic ESCM. Data in **a-d** are based on PI[2,3] and LGM[3,4] control runs. Data at (**e**, **g**) year 3,000 and (**f**, **h**) year 7,000 for (**e**, **f**) weakened NADW and (**g**, **h**) "NADW off" experiments performed with UVic ESCM. See Section 8.1 for simulation details.

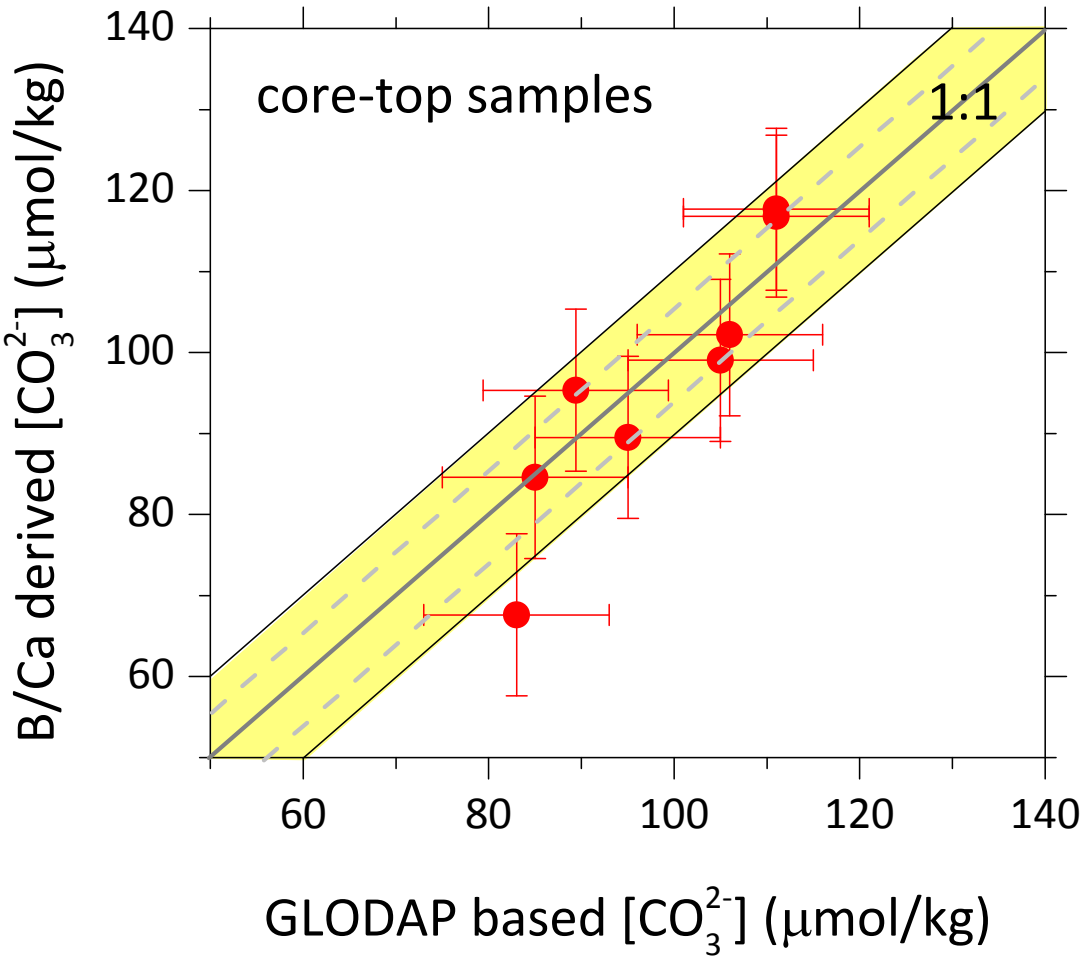

Supplementary Figure 3 | Comparison of core-top (<~5 ka) [CO_3^{2-}] estimated based on *C. wuellerstorfi* B/Ca and the GLODAP hydrographic dataset[1]. B/Ca-derived [CO_3^{2-}] (y-axis) are calculated using B/Ca = 1.14 * ([CO_3^{2-}] - [CO_3^{2-}]$_{saturation}$) + 177 (ref. [23]). Deep water [CO_3^{2-}] based on GLODAP (x-axis) are estimated using the nearby hydrographic sites after removing the anthropogenic CO_2 influences. Error bars show the ±2σ uncertainty, at ±10 µmol/kg for both y (based on the core-top calibration[23]) and x (arbitrarily assigned to take account of errors associated with hydrographic data[51]) values. The yellow band show ±10 µmol/kg envelope along the 1:1 line (grey line). The grey dashed lines are for the ±1σ uncertainty. Considering uncertainties, B/Ca-derived [CO_3^{2-}] results agree well with those based on the GLDOAP dataset. Note that hydrographic sites are not at the exact locations of the core-tops, and some uncertainties (~±5 µmol/kg in DIC and ALK) may be associated with hydrographic data measurements. Also, core-top samples may be up to 3-5,000 years old due to bioturbation, and sometimes are affected by short-lived localized conditions such as organic fluff[52].

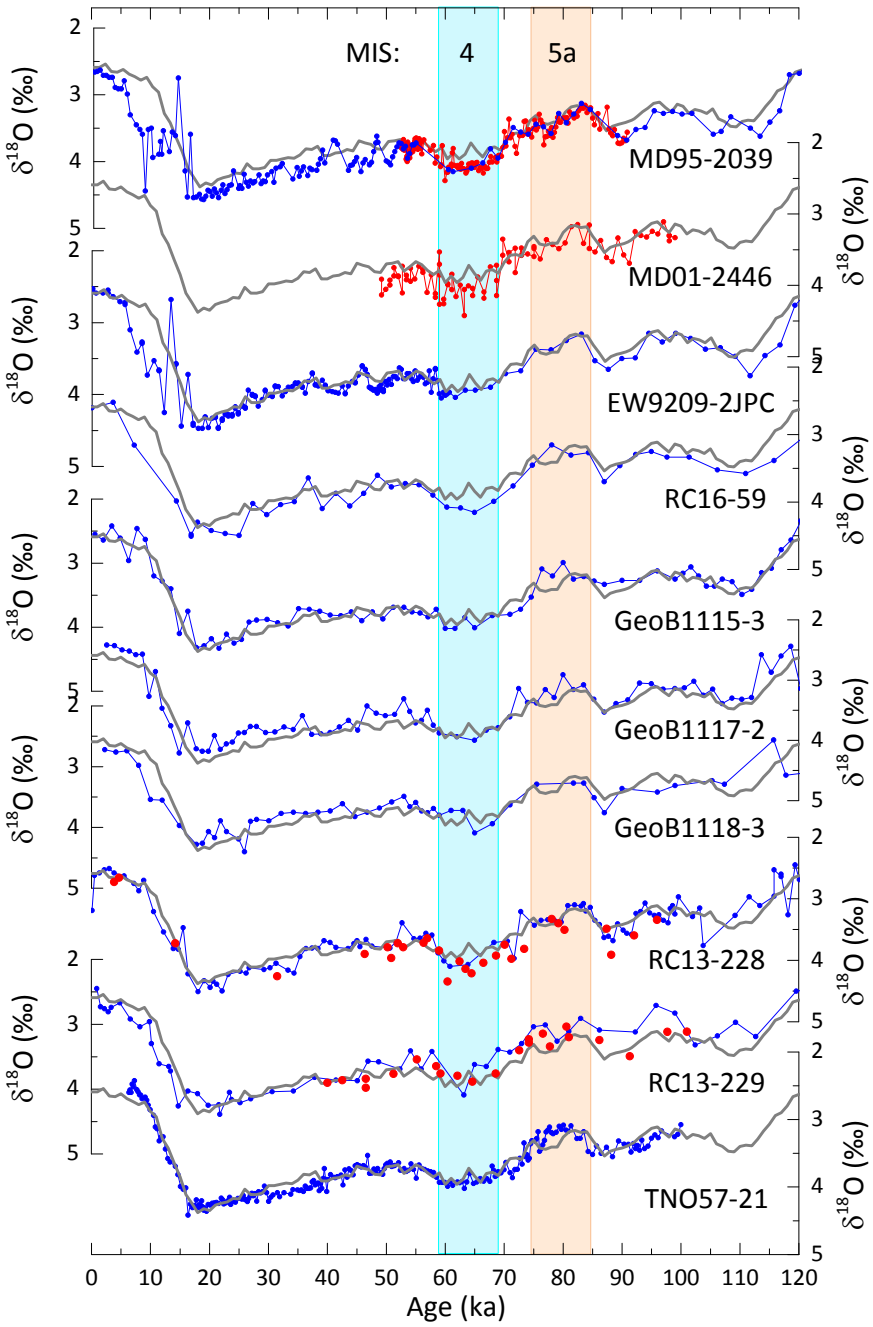

Supplementary Figure 4 | Chronology of cores used in this study. Grey curves are for the LR04 benthic $\delta^{18}O$ stack[30]. Blue curves are from the literature[16,19,31,53-56], and red symbols are from this study.

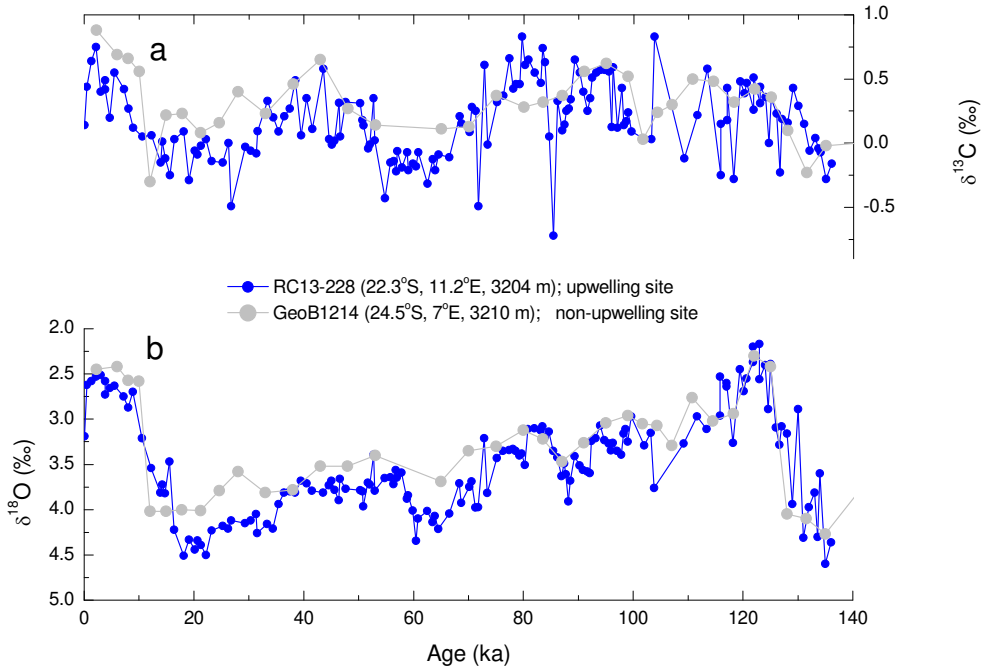

Supplementary Figure 5 | Comparison of benthic $\delta^{13}C$ in two nearby cores RC13-228 (upwelling site) and GeoB1214[32] (non-upwelling site) located at similar water depths. Except for the Holocene (~0-10 ka) and the last glacial period (~20-30 ka) when $\delta^{13}C$ in core RC13-228 show some lower values, benthic $\delta^{13}C$ are similar between the two cores during the last glacial cycle. The small offsets may be caused by age model uncertainties and the low resolution of GeoB1214.

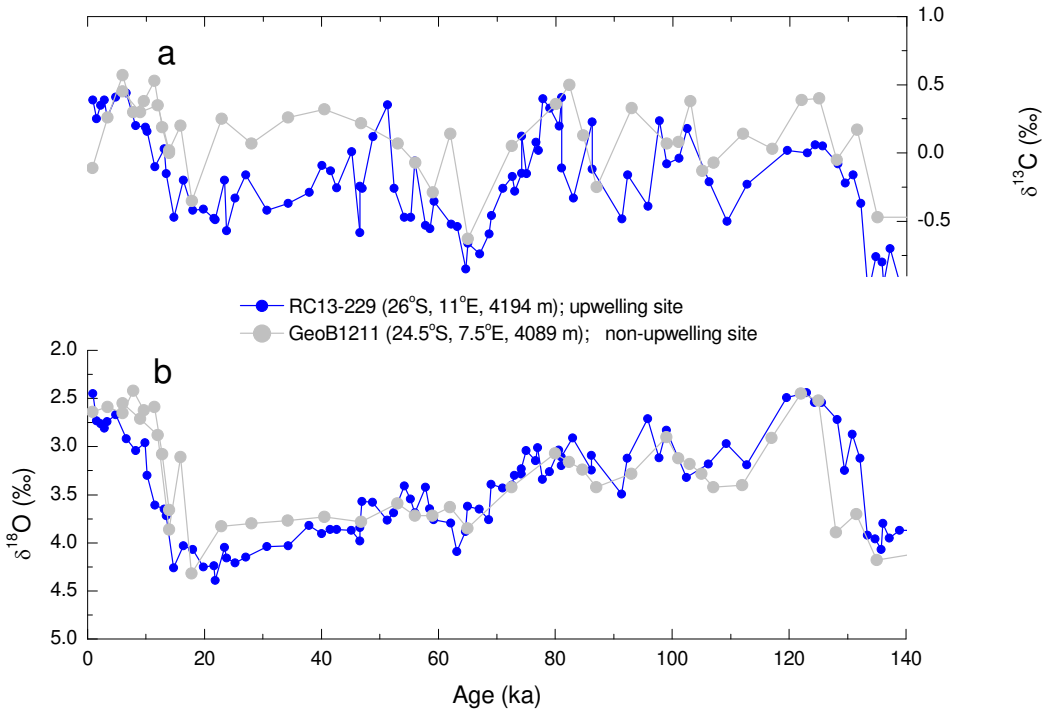

Supplementary Figure 6 | Comparison of benthic $\delta^{13}C$ for two nearby cores RC13-229 (upwelling site) and GeoB1211[32] (non-upwelling site) located at similar water depths. Considering the low-resolution record of GeoB1211 and age model uncertainties, benthic $\delta^{13}C$ in the two cores are comparable during the MSI 5a to MIS 4 transition. This suggests that bottom water chemistry at site RC13-229 was minimally affected by local surface productivity across the MIS 5a-4 transition.

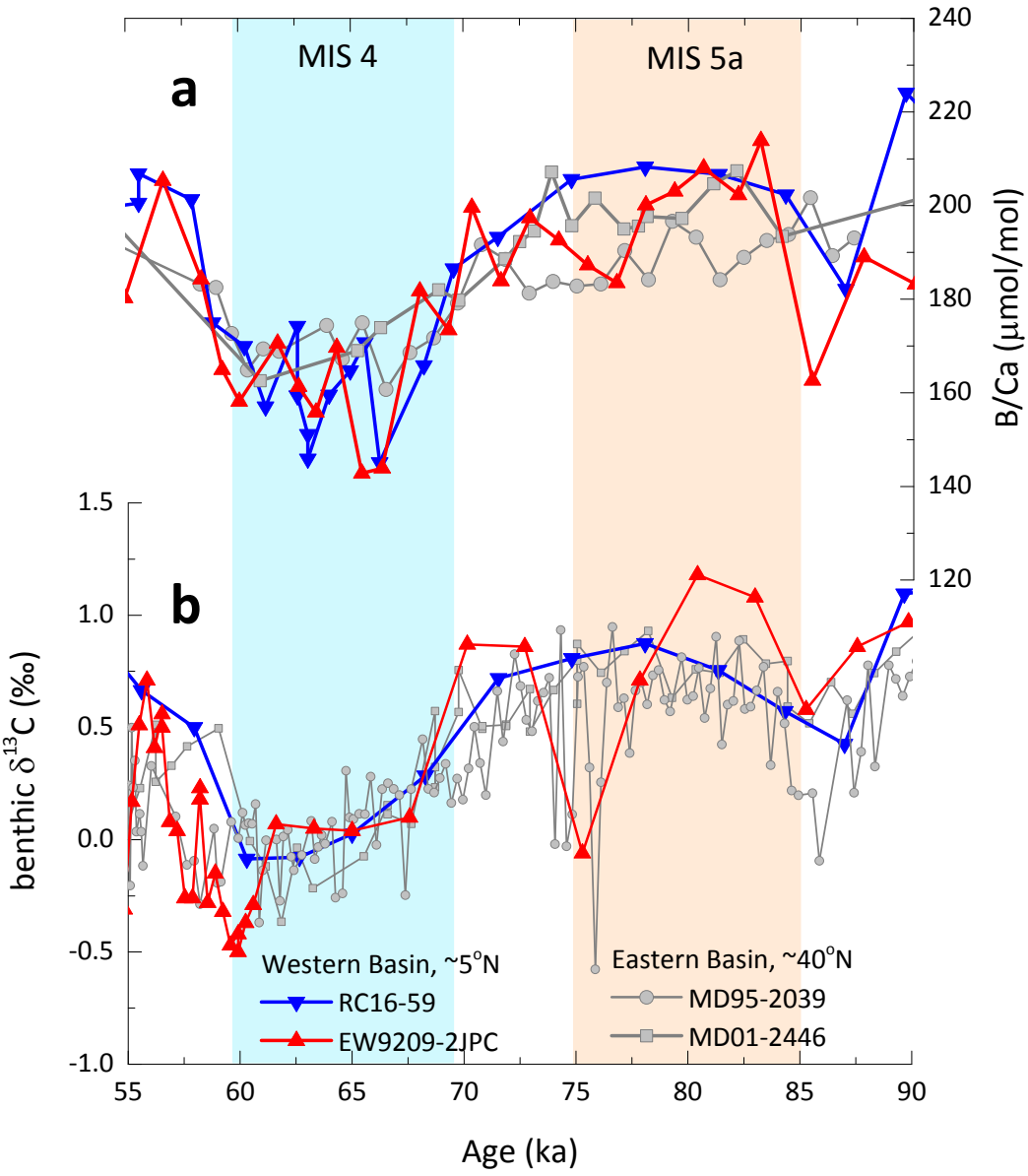

Supplementary Fig. 7 | Comparison of (a) benthic B/Ca and (b) $\delta^{13}C$ in cores from western and eastern basins in the North Atlantic Ocean. Compared to those from the eastern basin, cores from the western basin show larger changes in B/Ca, but similar variations in $\delta^{13}C$ (supplementary Table 4). Although we cannot entirely exclude other possibilities, at present our favored interpretation is a greater circulation change in the western basin during the transition from MIS 5a to 4 (Supplementary Fig 8). This would require a higher $\delta^{13}C$ of source waters filling in the western basin than those ventilating the eastern basin during MIS 4.

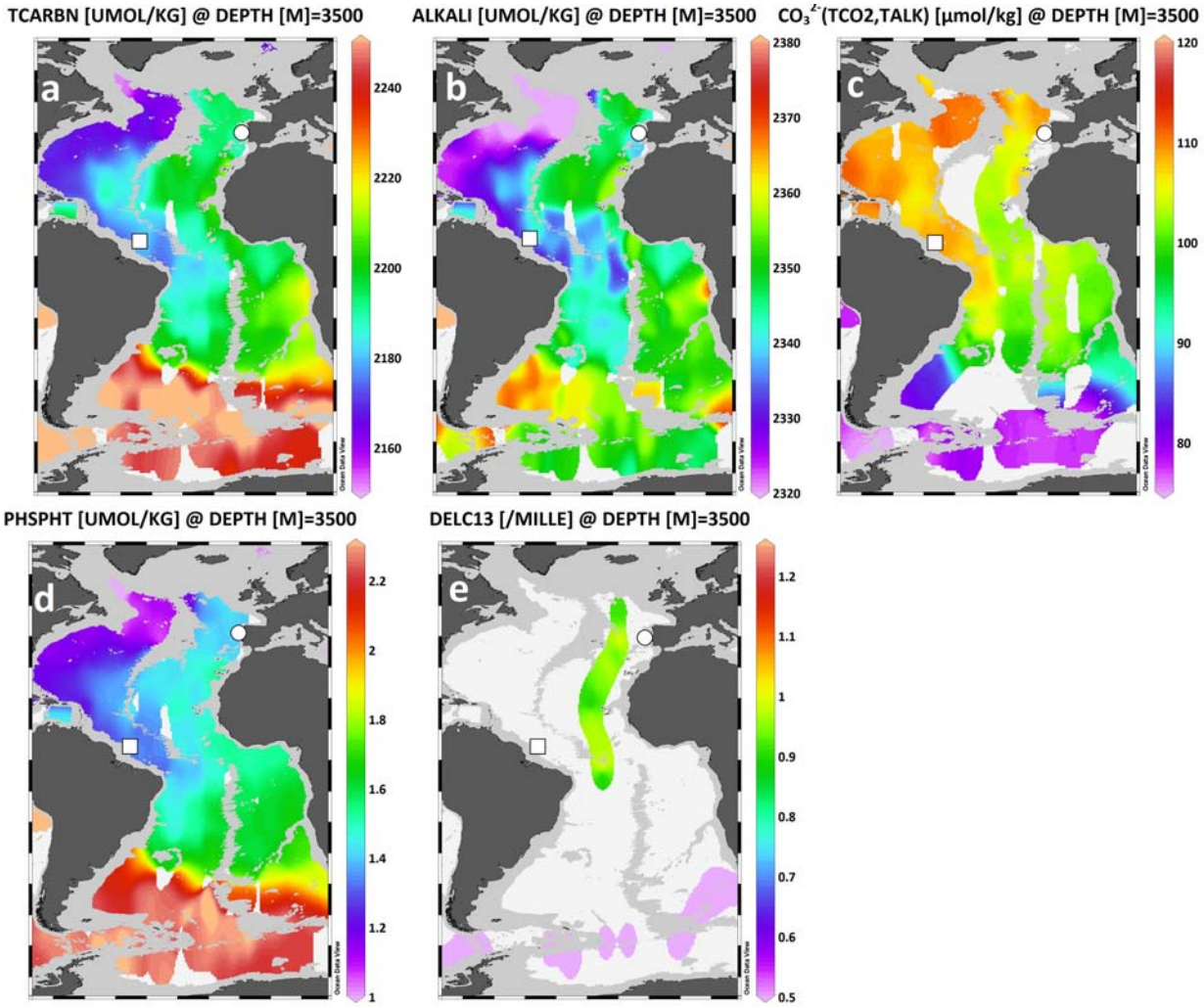

Supplementary Fig. 8 | Distributions of geochemical tracers at 3.5 km in the Atlantic Ocean based on the GLODAP dataset[1]. a, DIC. **b**, ALK, **c**, [CO_3^{2-}]. **d**, PO_4. **e**, $\delta^{13}C$. Square = RC16-59/EW9209-2JPC; circle = MD01-2336/MD95-2039. Compared to the eastern basin, the western North Atlantic at 3.5 km water depth generally shows lower DIC, ALK, PO_4 and higher [CO_3^{2-}]. Assuming the same end-member values of deep waters formed in the polar regions, this contrast suggests a greater proportion of NADW in the western basin at 3.5 km in the North Atlantic during the PI. Given shoaling of NADW during glacials[57,58], the deep Atlantic (>~3 km) would be mainly occupied by AABW (Fig. 1). In this case, the western basin would experience a larger change in ocean circulation and consequently a greater amplitude in deep water [CO_3^{2-}].

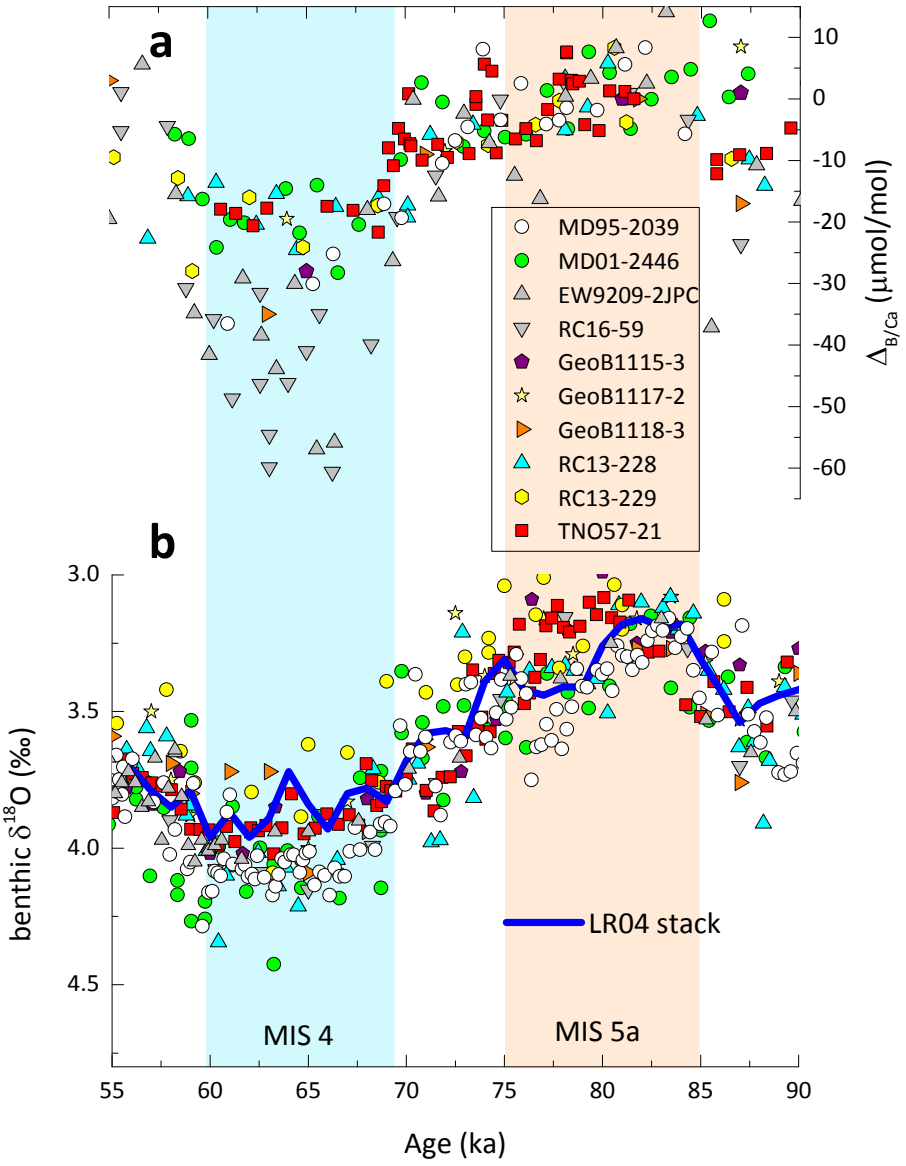

Supplementary Figure 9 | Comparison of changes in benthic B/Ca and $\delta^{18}O$. Changes in benthic B/Ca ($\Delta_{B/Ca}$) and $\delta^{18}O$ in each core are mirrored in that low benthic B/Ca correspond to heavy benthic $\delta^{18}O$, and vice versa. Specifically, the ~0.75‰ increase in $\delta^{18}O$ from MIS 5a to MIS 4 is accompanied with roughly 28 μmol/mol decline in benthic B/Ca.

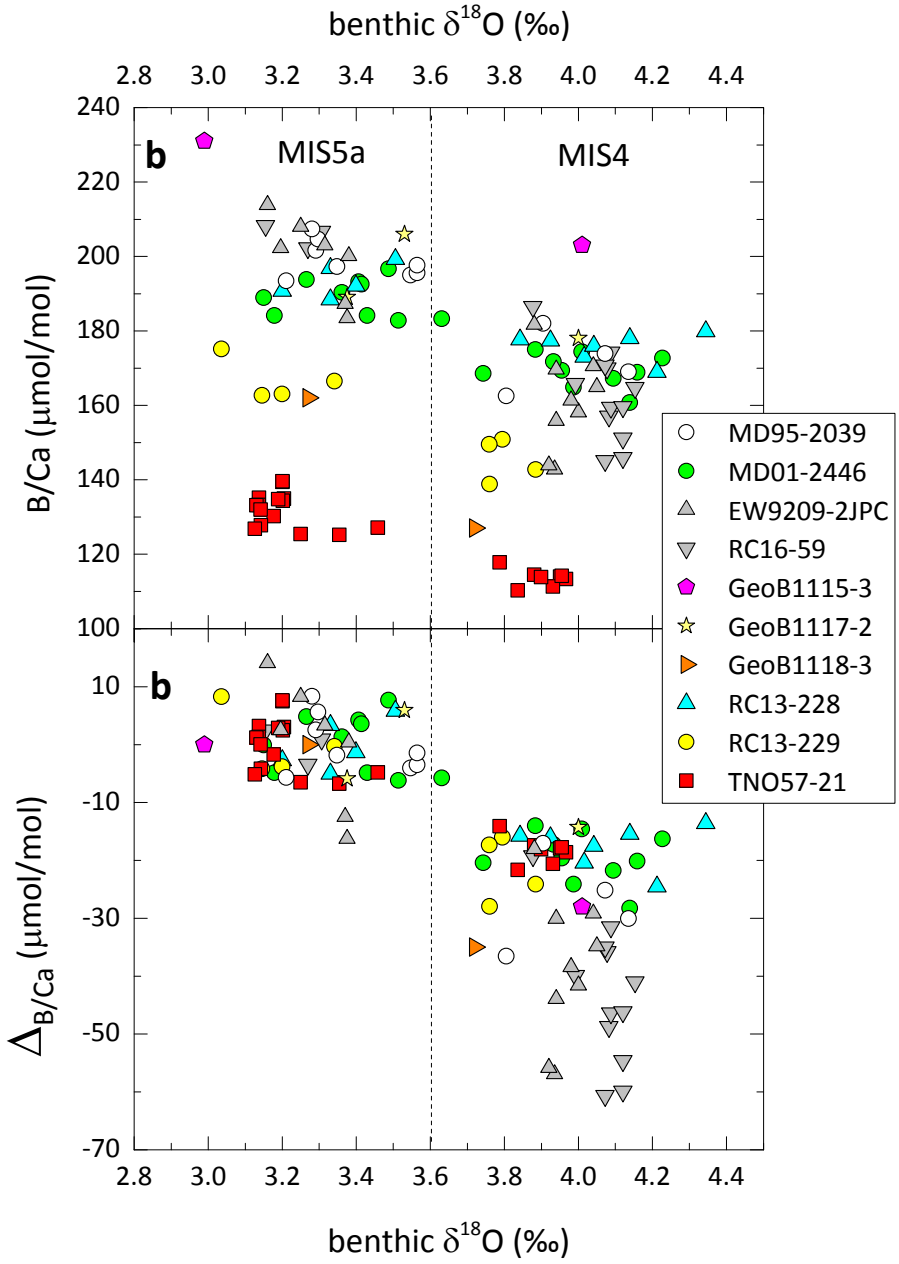

Supplementary Figure 10 | Correlation between benthic B/Ca and $\delta^{18}O$ for MIS 4 and MIS 5a. **a**, Benthic B/Ca vs. benthic $\delta^{18}O$. **b**, Benthic $\Delta_{B/Ca}$ vs. benthic $\delta^{18}O$. $\Delta_{B/Ca}$ = B/Ca - mean $B/Ca_{MIS\ 5a}$. Changes in benthic B/Ca are negatively correlated with benthic $\delta^{18}O$ in each core. Compared to MIS 5a, benthic for the 10 studied cores B/Ca is on average lowered by ~28 µmol/mol, corresponding to ~25 µmol/kg decrease in deep water $[CO_3^{2-}]$.

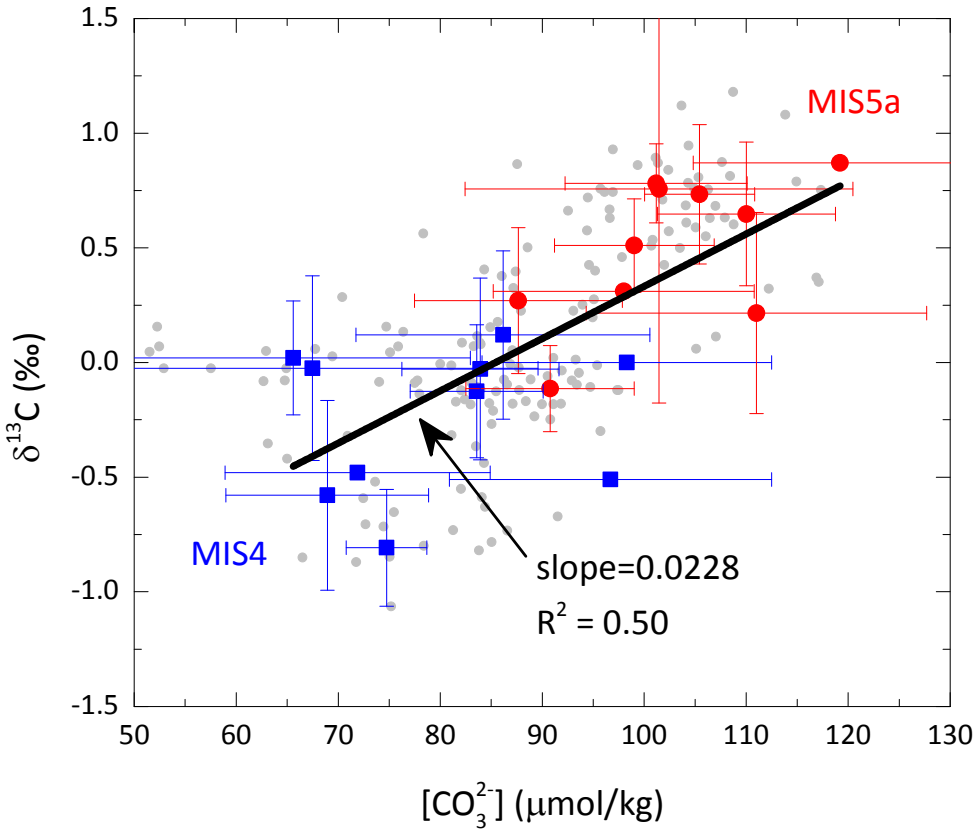

Supplementary Figure 11 | Deep water $\delta^{13}C$ vs. $[CO_3^{2-}]$ for 10 studied cores during MIS 5a and MIS 4. Red circles represent data for MIS 5a, and blue squares are for MIS 4 data. Error bars denote 2 standard deviations of data within the designated time interval (Supplementary Table 4). The bold black line represent the best linear fit of the data. If this trend is also applicable to other locations in the deep Atlantic, the average 0.45‰ decline in benthic $\delta^{13}C$ revealed by the stack curves (Supplementary Fig. 12) would indicate a $[CO_3^{2-}]$ decline of ~20 μmol/kg in the deep Atlantic from MIS 5a to MIS 4. This change is similar to the value (~25 μmol/kg) revealed by $[CO_3^{2-}]$ reconstructions based on benthic B/Ca for the 10 studied cores (Fig. 2, 3, and Supplementary Table 4). Small grey circles are paired $[CO_3^{2-}]$-$\delta^{13}C$ from MIS 5a to MIS 4 (85-59 ka)

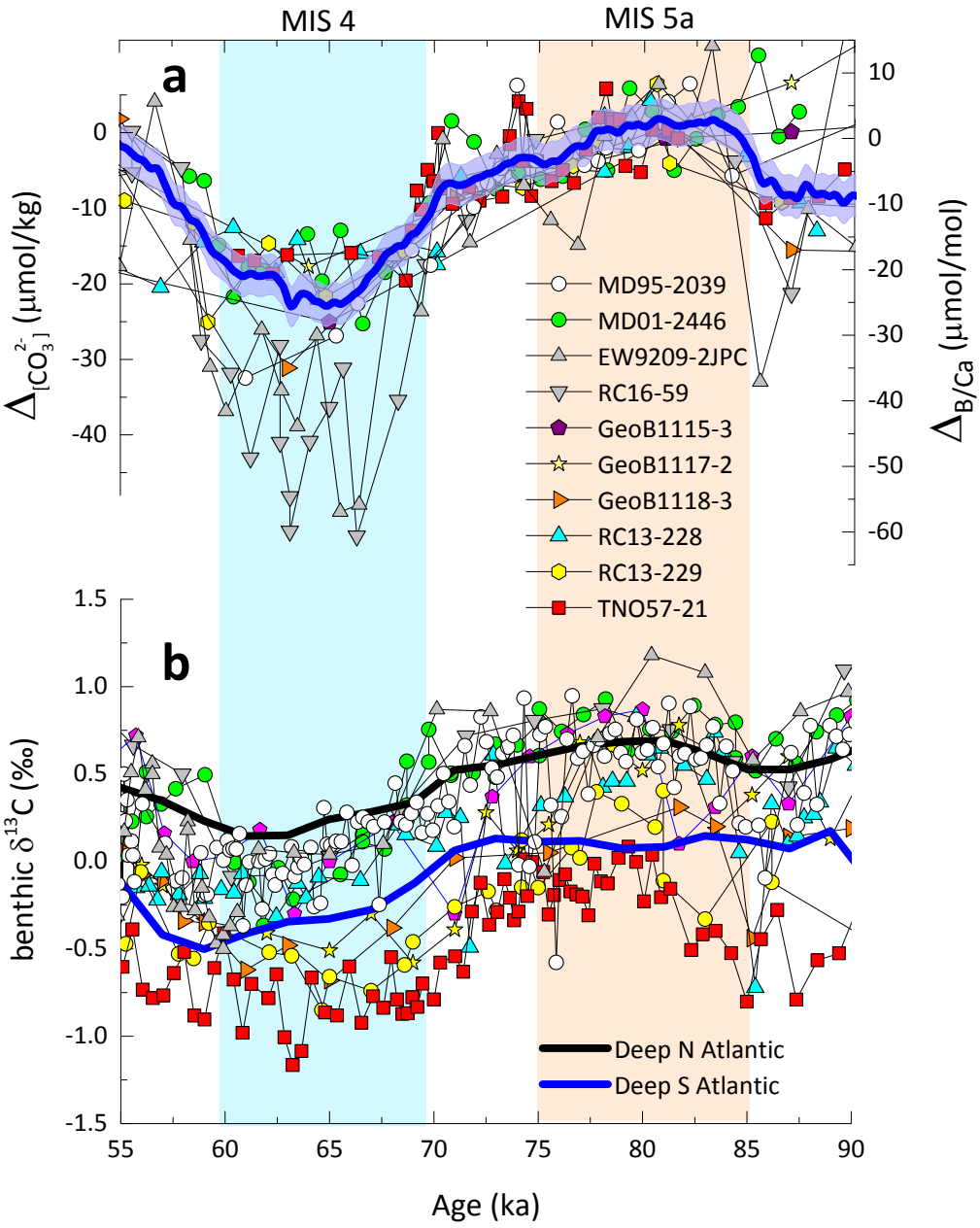

Supplementary Figure 12 | Comparison of B/Ca and benthic $\delta^{13}C$. **a**, $\Delta_{B/Ca}$ and corresponding $\Delta_{[CO_3^{2-}]}$ (see Fig. 3c). **b**, benthic $\delta^{13}C$. In each core, $\Delta_{B/Ca}$ and $\delta^{13}C$ are positively correlated. Also shown in (**b**) are benthic $\delta^{13}C$ stack curves for the deep N (north of 45°S; bold black curve) and S (south of 45°S; bold blue curve) Atlantic[59]. Note that the stack curves are normalized to the LGM values (i.e., LGM $\delta^{13}C$ = 0‰). These stack records show ~0.45‰ decline in $\delta^{13}C$ from MIS 5a to MIS 4.

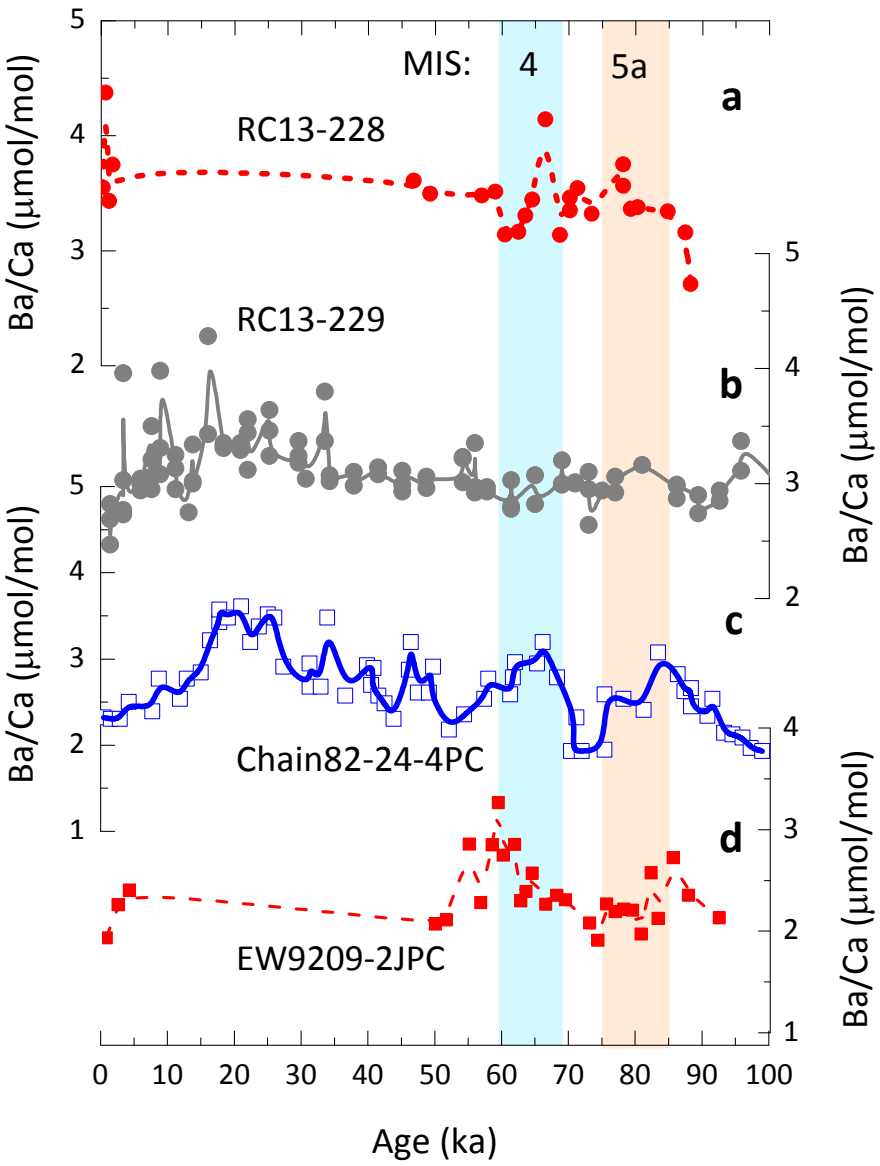

Supplementary Figure 13 | Benthic Ba/Ca in 4 cores from the deep Atlantic. **a**, RC13-228 (this study). **b**, RC13-229[60]. **c**, Chain82-24-4PC[61]. **d**, EW9209-2JPC (this study). In all 4 cores, no Ba/Ca decline is observed from MIS 5a to MIS 4. Instead, data from 3 out of 4 cores show some signs of Ba/Ca increases (up to ~25%) during MIS 4 (**a, c, d**).

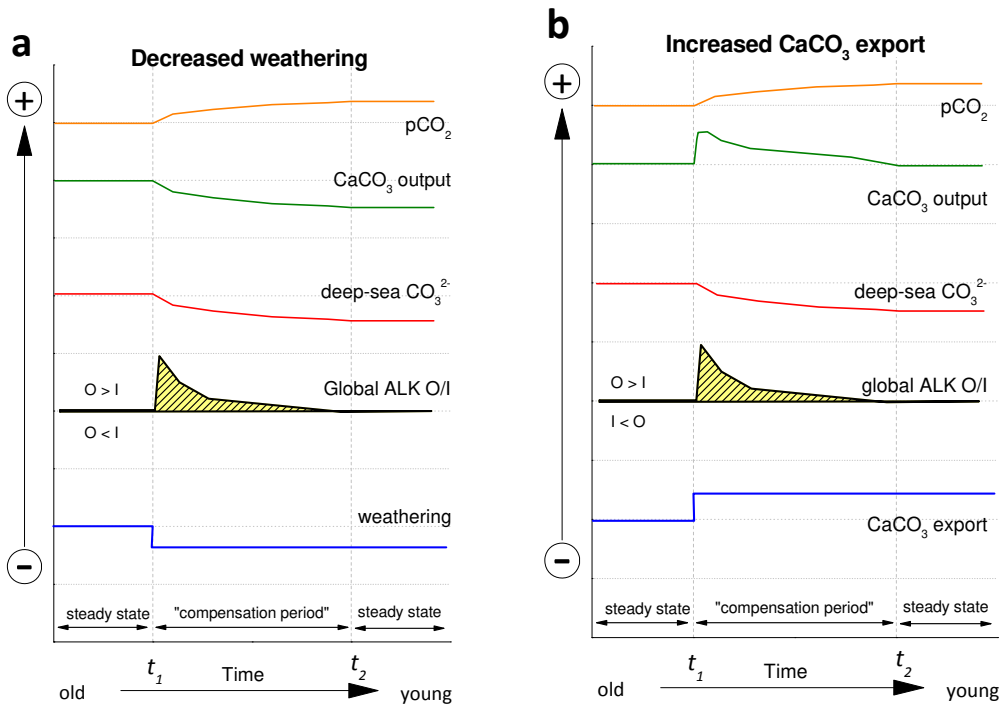

Supplementary Figure 14 | Schematic diagrams showing the global mean deep water [CO_3^{2-}] changes in response to (a) a step decline in carbonate weathering, and (b) a step increase in surface $CaCO_3$ export. Also shown include the global ALK output/input (O/I) ratio (black), deep-sea $CaCO_3$ burial (olivine), and atmospheric pCO_2 changes (orange).

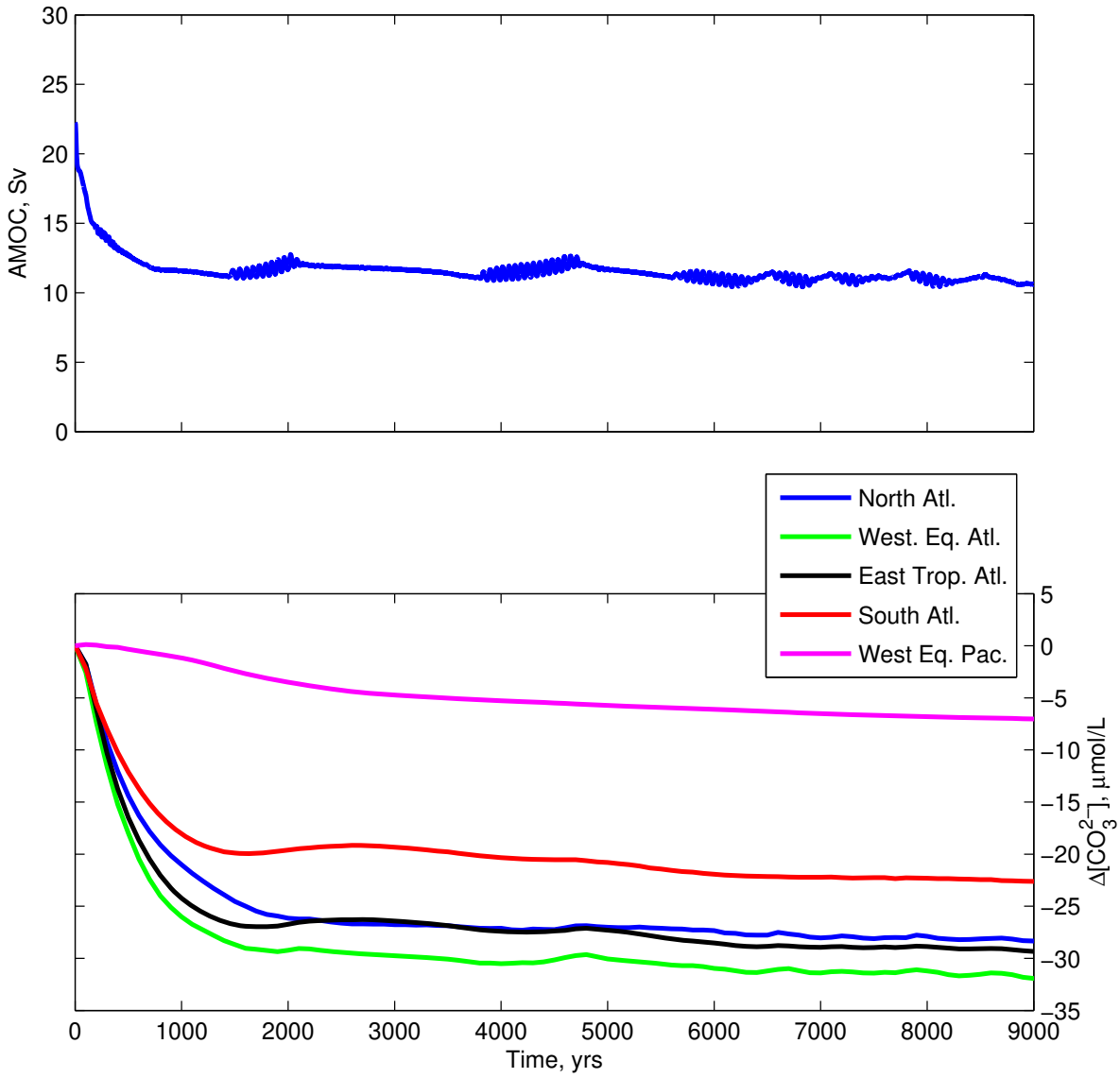

Supplementary Figure 15 | Timeseries of (top) NADW (Sv) and (bottom) deep water [CO_3^{2-}] anomalies (µmol/kg) as simulated by the UVic ESCM. In the bottom panel, curves represent the averaged values for the North Atlantic (blue, 37°N-42°N, 15°W-5°W, 3600m), the Western Equatorial Atlantic (green, 0°-6°N, 45°W-40°W, 3200m), the Eastern Tropical Atlantic (black, 25°S-5°S, 0°-15°E, 3600m), the South Atlantic (red, 45°S-40°S,0°-10°E, 3600m) and the Western Equatorial Pacific (magenta, 0-10°N,130°E-160°E, 3600m).

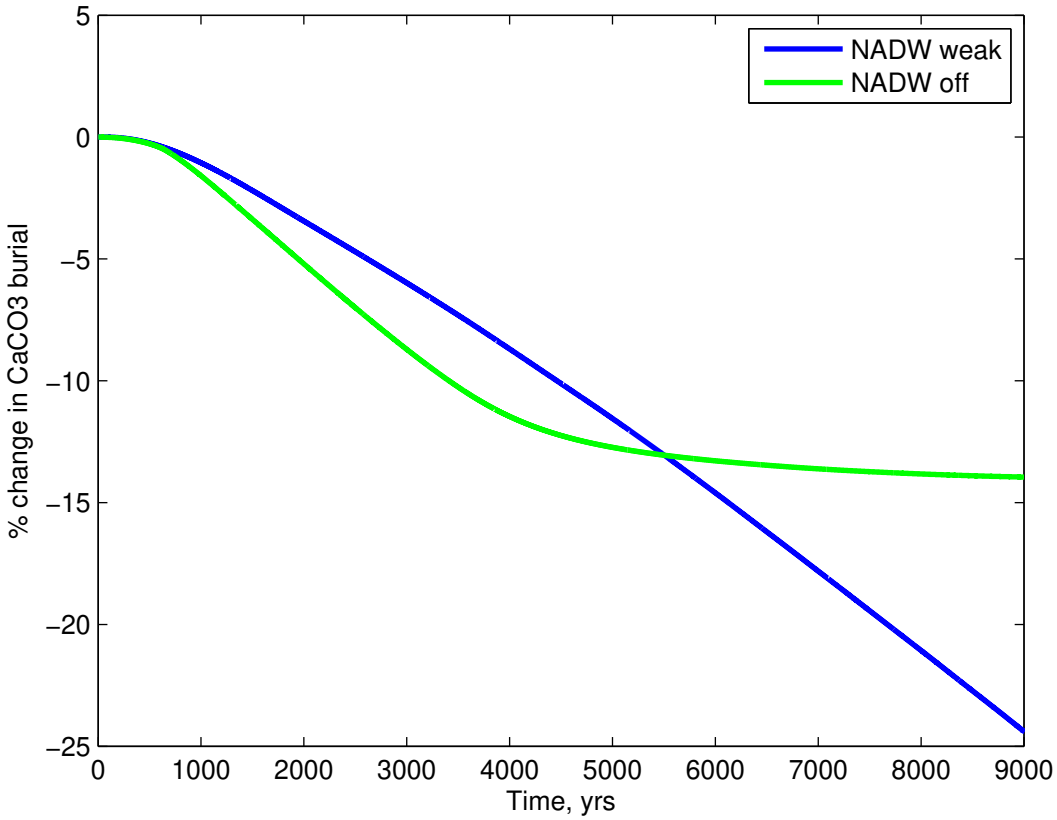

Supplementary Figure 16 | Timeseries of percent change in $CaCO_3$ burial in the experiment with NADW halved (blue) and the one with NADW cessation (green) performed with the UVic ESCM.

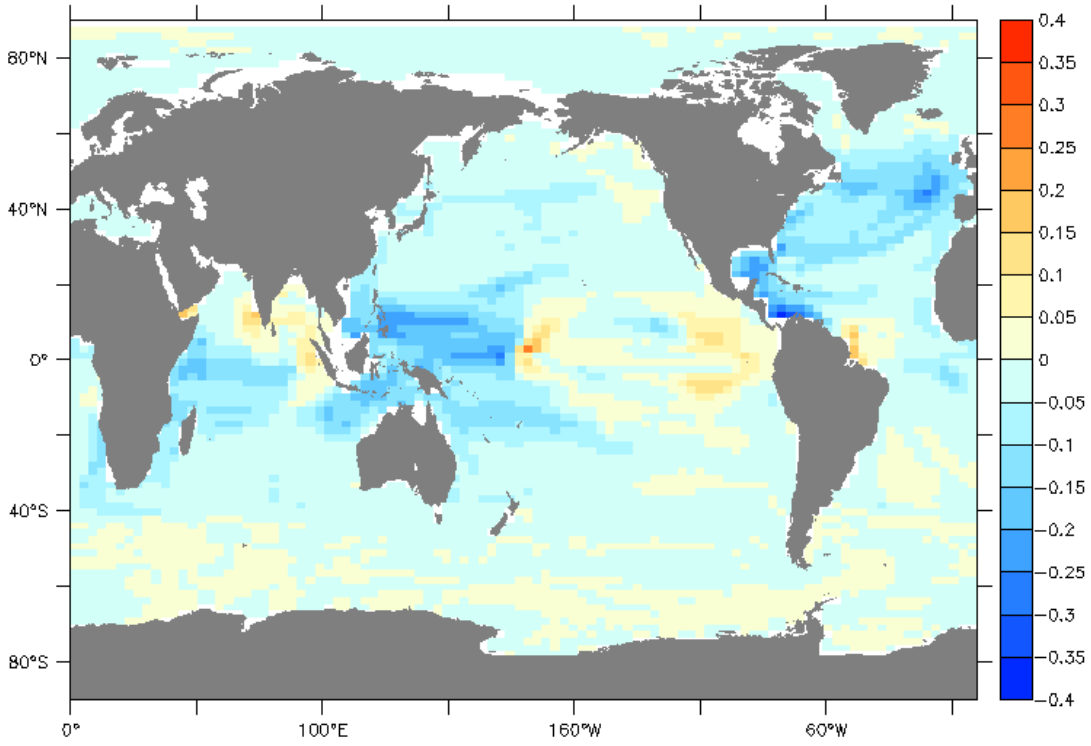

Supplementary Figure 17 | $CaCO_3$ export anomalies (mol C/m^2/yr) at year 7,000 compared to the control in the halved NADW experiment performed with the UVic ESCM.

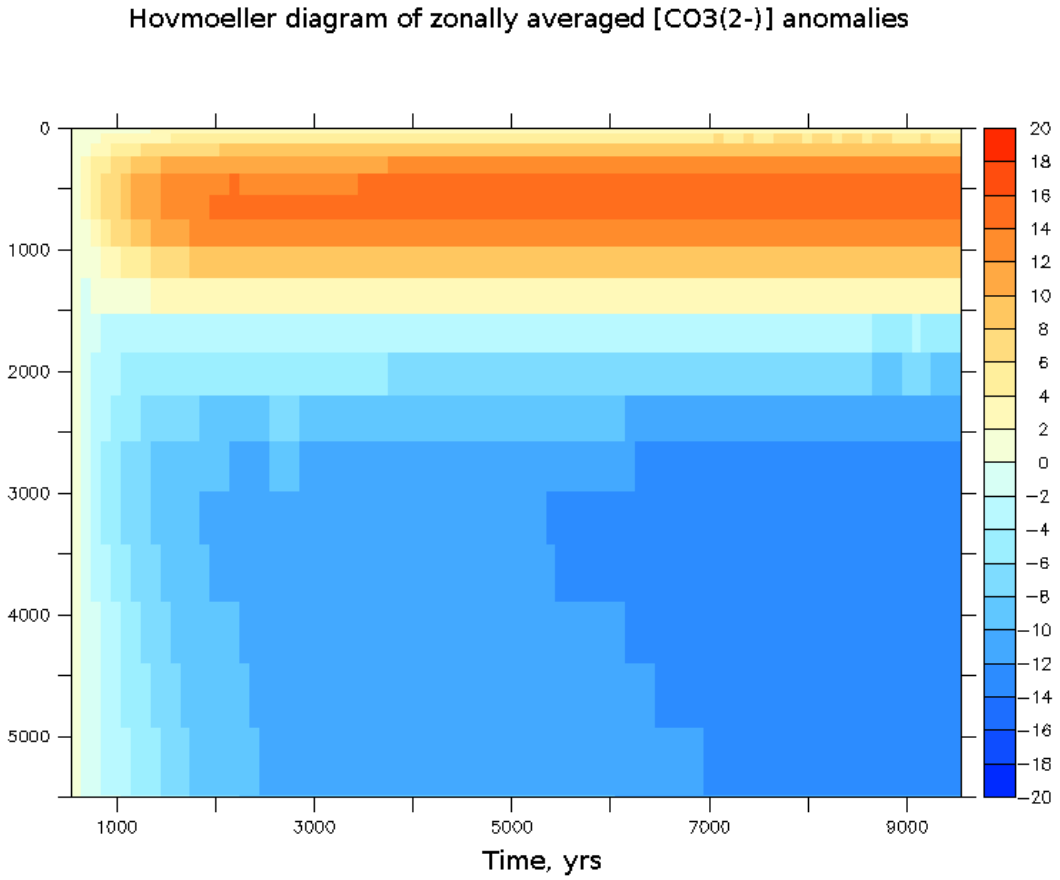

Supplementary Figure 18 | Hovmoeller diagram of the globally averaged [CO_3^{2-}] anomalies (µmol/kg) in the halved NADW experiment performed with the UVic ESCM. The y axis represents depth (m) and the x axis time (years).

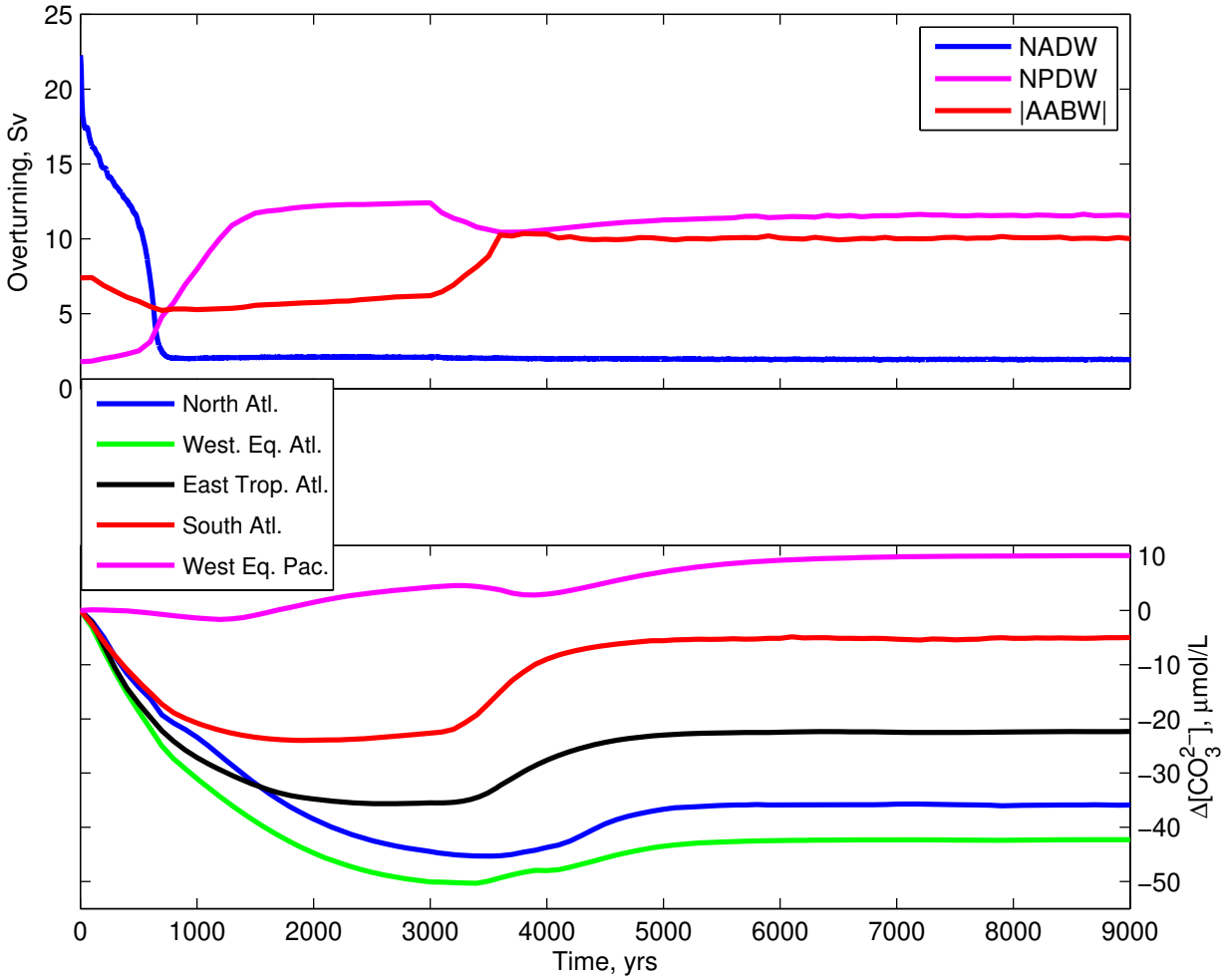

Supplementary Figure 19 | Timeseries of (top) overturning circulation (Sv) and (bottom) [CO_3^{2-}] anomalies (µmol/kg) as simulated by the UVic ESCM. The top panel shows changes in NADW (blue), NPDW (magenta) and AABW (red). In the bottom panel shows the averaged anomalies for the North Atlantic (blue, 37°N-42°N, 15°W-5°W, 3600m), the Western Equatorial Atlantic (green, 0°-6°N, 45°W-40°W, 3200m), the Eastern Tropical Atlantic (black, 25°S-5°S, 0°-15°E, 3600m), the South Atlantic (red, 45°S-40°S,0°-10°E, 3600m) and the Western Equatorial Pacific (magenta, 0°-10°N,130°-160°E, 3600m).

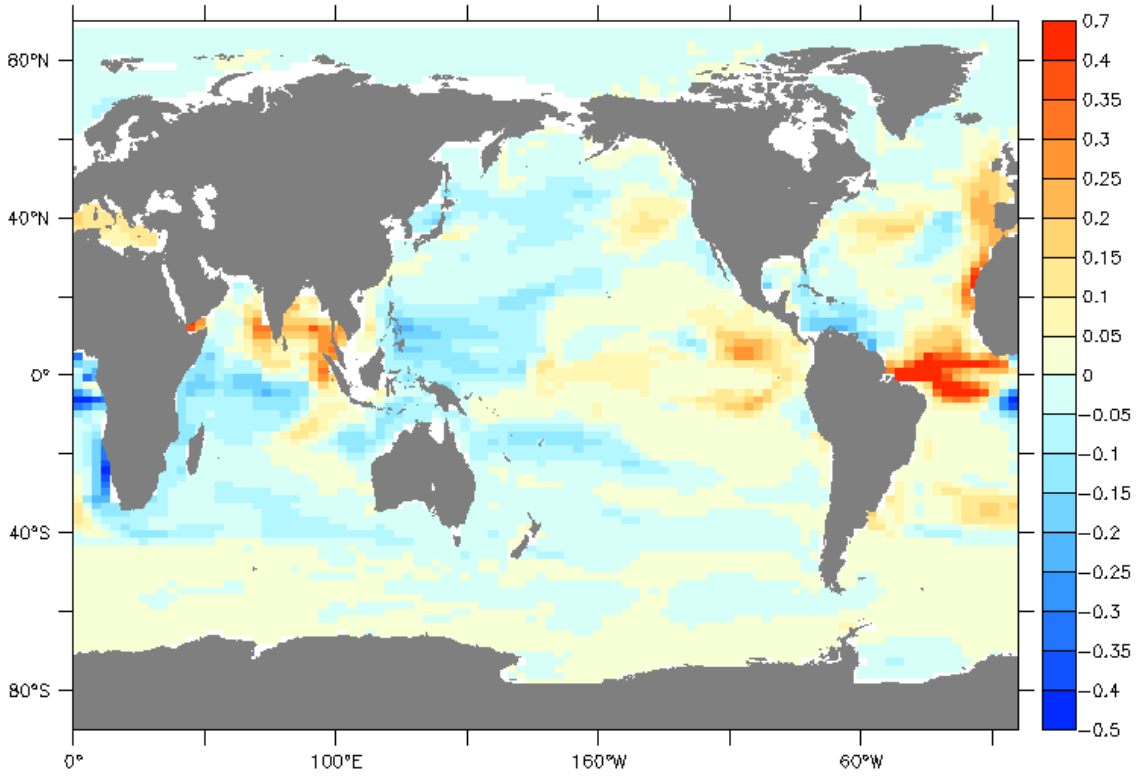

Supplementary Figure 20 | $CaCO_3$ export anomalies (mol C/m^2/yr) at year 7,000 compared to control in the NADW off experiment by UVic ESCM.

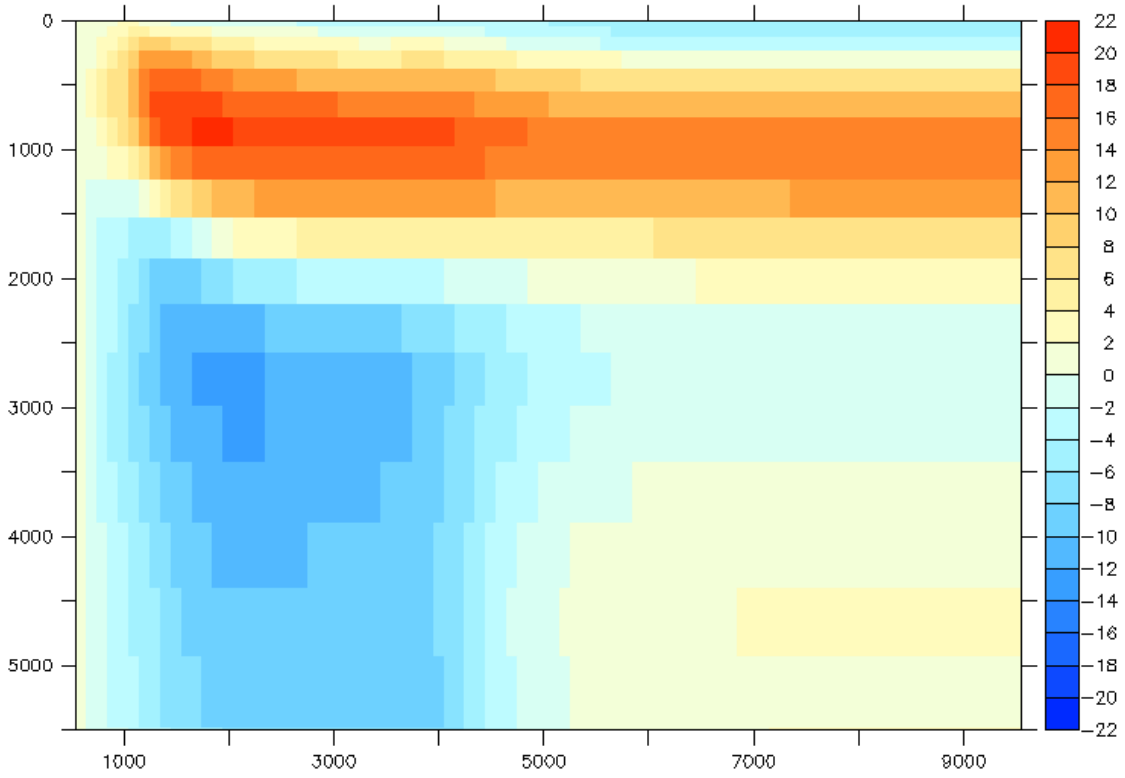

Supplementary Figure 21 | Hovmoeller diagram of the globally averaged [CO_3^{2-}] anomalies (µmol/kg) in the "NADW off" experiment by UVic ESCM. The y axis represents depth (m) and the x axis time (years).

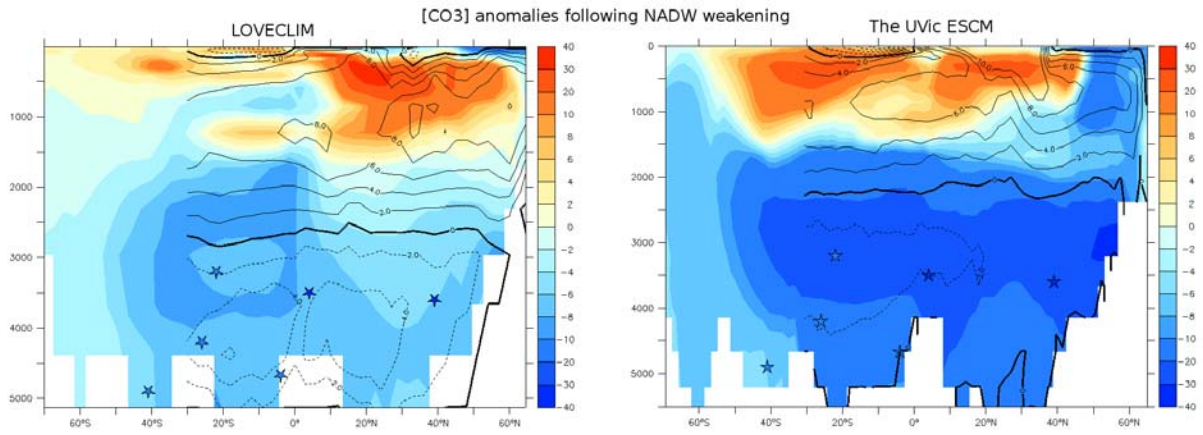

Supplementary Figure 22 | Modeled [CO_3^{2-}] results. Seawater [CO_3^{2-}] anomalies (µmol/kg; color shading) at year 1,000 due to a 50% weakening of NADW under constant pre-industrial condition as simulated by (**left**) LOVECLIM and (**right**) the UVic ESCM. Overlaid contours show the Atlantic Meridional Overturning stream function (Sv) with weak and shallow NADW above ~2.5 km water depth and Southern Sourced bottom waters below. Stars represent [CO_3^{2-}] anomalies recorded in marine sediment cores described in this study across the MIS 5a-4 boundary. Cores from North to South are MD95-2039, RC16-59, GEOB1118-3, RC13-228, RC13-229, and TNO57-21.

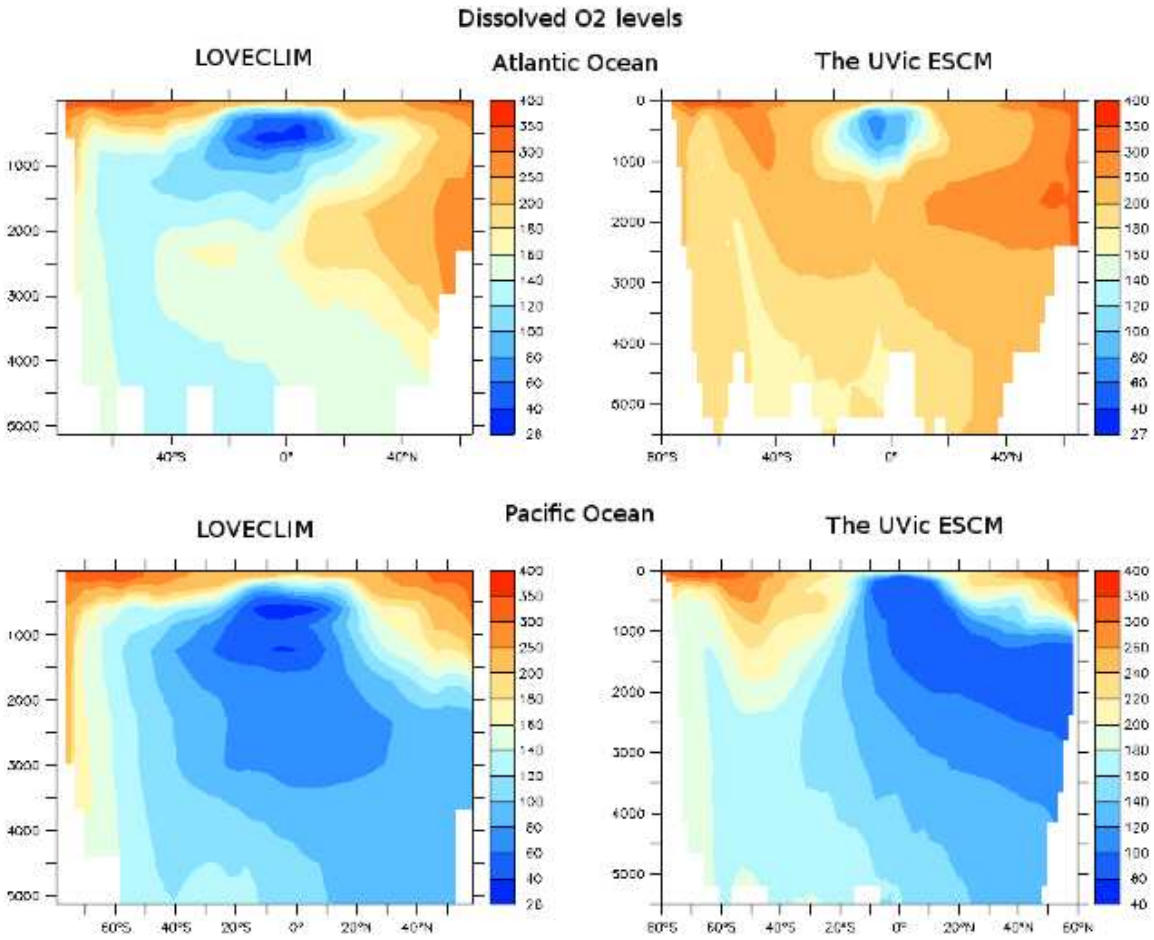

Supplementary Figure 23 | Simulated dissolved O_2 levels (μmol/kg) in the Atlantic Ocean (top) and the Pacific Ocean (bottom) at model year 1,000 in halved-NADW experiments performed with (left) LOVECLIM and (right) the UVic ESCM.

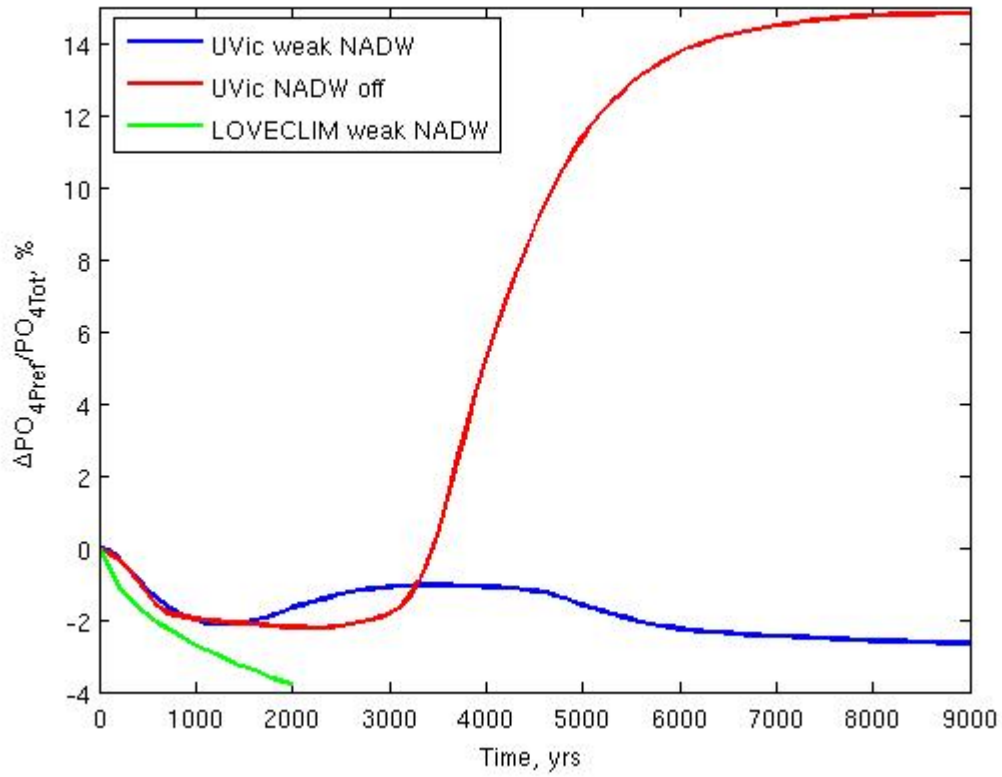

Supplementary Figure 24 | Time series of globally averaged preformed phosphate over total phosphate (%) for experiments performed with the UVic ESCM for a 50% weakening of NADW (blue) and NADW off (red), compared to a 50% NADW weakening performed with LOVECLIM (green).

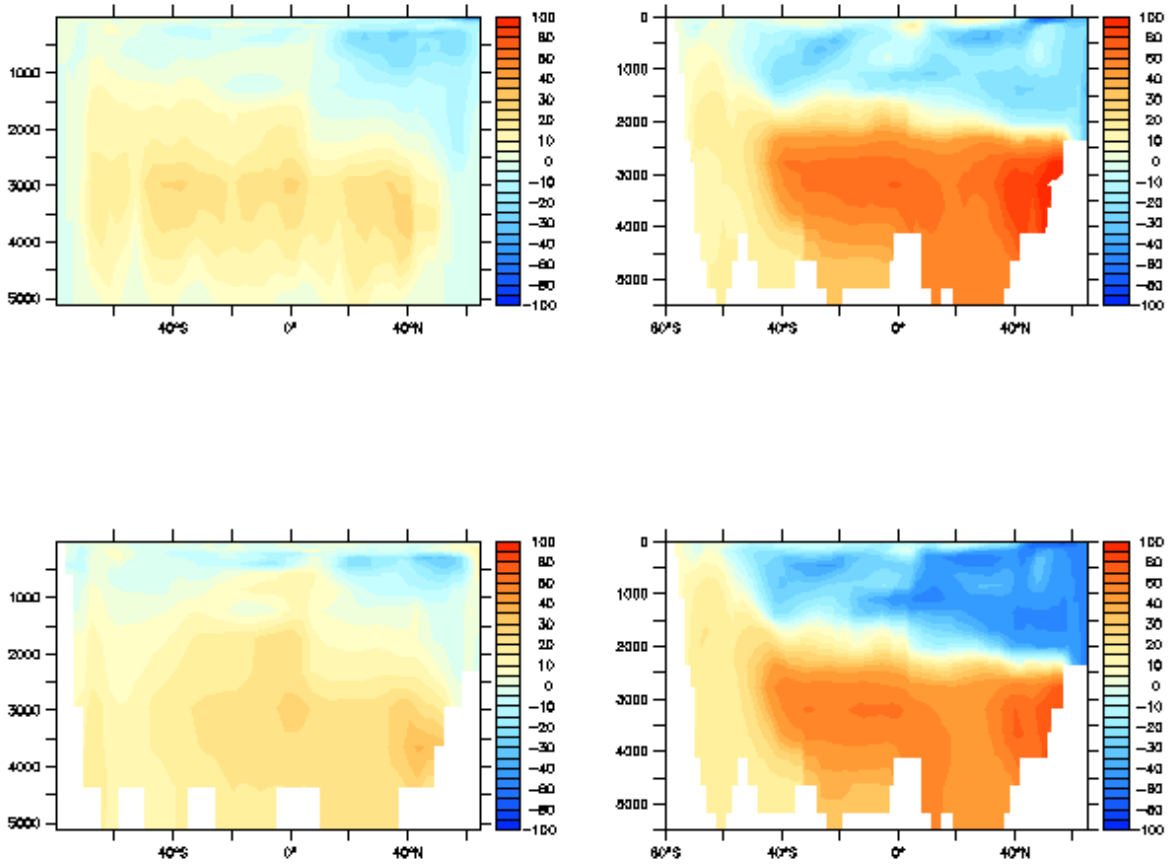

Supplementary Figure 25 | (top) DIC anomalies (μmol/kg) and (bottom) C_{soft} anomalies (μmol/kg) averaged over the Atlantic basin during NADW weakening in (left) LOVECLIM and (right) the UVic ESCM compared to the pre-industrial control runs.

Supplementary Tables:

Table 1. Locations, sedimentation rates and preindustrial (PI) deep water [CO_3^{2-}] and saturation [CO_3^{2-}] for cores used in this study. PI and saturation [CO_3^{2-}] are estimated based on the GLODAP dataset[1].

Label in Fig.1	core	Lat	Long	water depth	Sed. rate	PI CO_3^{2-}	$[CO_3^{2-}]_{sat}$	$[CO_3^{2-}]$
		°N	°W	m	cm/kyr	μmol/kg	μmol/kg	data source
a	MD95-2039	40.6	10.3	3381	9.5	105	84	This study
b	MD01-2446	39	12.6	3576	5.2	105	85	This study
c	EW9209-2JPC	5.64	44.47	3528	4.8	111	87	This study
d	RC16-59	4	43	3520	3.6	111	87	[16] & this study
h	RC13-228	-22.3	-11.2	3204	5.2	95	79	This study
i	RC13-229	-25.5	-11.3	4191	2.6	85	96	This study
j	TNO57-21	-41.1	-7.8	4981	15.0	83	115	This study
e	GeoB1115	-3.56	12.56	2945	3.3	106	75	[26]
f	GeoB1117	-3.81	14.89	3984	3.3	98	92	[26]
g	GeoB1118	-3.56	16.42	4671	2.6	89	105	[26]

Table 2. Age models for cores used in this study, based on comparisons of benthic $\delta^{18}O$ with the LR04 stack curve[30].

Event	Age	MD95-2039	MD01-2446	EW9209-2JPC	RC16-59	RC13-228	RC13-229
	ka	cm	cm	cm	cm	cm	cm
top	0.1	0	0	1	0	0	0
LGM	18	351	115	63	50	107	55
peak MIS 4	65	1522	383	340	250	338	185
peak MIS 5a	83	1662	451	410	305	417	230
mid MIS 5c	99	1765	517	480	365	520	255
peak MIS 5e	123	1910		575	415	620	290
MIS 6	136	2020		605	450	685	340

Table 3. Depth and age ranges used to calculate averages of benthic B/Ca and $\delta^{13}C$ and deep water [CO_3^{2-}] for MIS 5a and MIS 4.

core	MIS 5a		MIS 4	
	depth range (cm)	age range (ka)	depth range (cm)	age range (ka)
MD95-2039	1604-1671	76-84	1468-1555	61-69
MD01-2446	420-458	75-85	352-398	59-69
EW9209-2JPC	380-412	75-83	306-353	59-68
RC16-59	290-310	78-85	230-260	60-69
RC13-228	395-429	78-85	308-355	59-69
RC13-229	213-227	79-87	168-195	59-69
TNO57-21	1127-1219	75-82	916-1014	60-69
GeoB1115	248-249	81	213-214	65
GeoB1117	278-299	72, 87	233-234	64
GeoB1118	218-219	82	188-189	63

Table 4. Average benthic B/Ca and $\delta^{13}C$ and deep water [CO_3^{2-}] for MIS 5a and MIS 4.

Core	B/Ca μmol/mol	1sd***	CO_3^{2-} μmol/kg	1sd***	$\delta^{13}C$ ‰	1sd	n
Average for MIS 5a (75-85 ka)							
MD95-2039	199.1	5.0	110.0	4.4	0.65	0.16	8
MD01-2446	189.0	5.1	101.2	4.5	0.78	0.09	10
EW9209-2JPC*	199.7	10.8	101.4	9.5	0.76	0.47	7
RC16-59*	205.8	3.1	105.4	2.7	0.73	0.15	3
RC13-228	193.4	4.5	99.0	3.9	0.51	0.10	5
RC13-229	166.8	5.8	87.7	5.1	0.27	0.16	4
TNO57-21	131.9	4.7	90.8	4.1	-0.11	0.09	15
GeoB1115	231.0	7.0	119.2	7.2	0.87		1
GeoB1117	197.5	12.0	111.0	8.3	0.22	0.22	2
GeoB1118*	162.0	6.0	98.0	6.4	0.31		1
Average for MIS 4 (59-69 ka)							
MD95-2039	171.9	8.2	86.2	7.2	0.12	0.18	4
MD01-2446	169.3	4.4	83.9	3.9	-0.03	0.20	10
EW9209-2JPC*	161	12.6	67.5	11.1	-0.03	0.2	9
RC16-59*	160.3	9.9	65.6	8.7	0.02	0.12	11
RC13-228	175.8	3.7	83.6	3.3	-0.13	0.14	7
RC13-229	145.5	5.7	68.9	5.0	-0.58	0.21	4
TNO57-21	113.6	2.3	74.7	2.0	-0.81	0.13	8
GeoB1115	203.0	7.0	98.3	7.1	0.00		1
GeoB1117	178.0	7.0	96.7	7.9	-0.51		1
GeoB1118*	127.0	6.0	71.9	6.5	-0.48		1
Difference between MIS5a and MIS4 averages							
MD95-2039	27.2	9.6	23.9	8.5	0.53	0.24	
MD01-2446	19.6	6.7	17.2	5.9	0.81	0.22	
EW9209-2JPC*	38.7	16.6	34	14.6	0.78	0.51	
RC16-59*	45.4	10.4	39.9	9.2	0.71	0.20	
RC13-228	17.6	5.8	15.5	5.1	0.64	0.18	
RC13-229	21.4	8.1	18.7	7.1	0.85	0.26	
TNO57-21	18.3	5.2	16.0	4.6	0.69	0.16	
GeoB1115	28.0	9.9	24.6	8.7	0.87		
GeoB1117	19.5	13.9	17.1	12.2	0.73	0.22	
GeoB1118*	35.0	8.5	30.7	7.5	0.79		
Mean of MIS 5a and MIS 4 differences**							
Mean of western basin	39.7	11.8	34.8	10.5	0.76	0.23	
Mean of eastern basin	21.7	8.5	19.0	7.5	0.73	0.18	
Mean of all cores	27.1	9.5	23.8	8.4	0.74	0.20	

*: Cores from the western basin.

**: The mean values represented here are generally similar to those shown in Fig. 3a. The small difference is due to different calculation methods. The values here are the means of the averaged differences between MIS 5a and MIS 4 of individual cores, while those shown in Fig 3a are calculated based on data from all relevant cores for the designated time periods.

***: See Section 3 for calculation method.

Supplementary Tables 5- 11 given in a separate Excel file list all new data presented in this study.

References

1. Key, R. M. et al. A global ocean carbon climatology: Results from Global Data Analysis Project (GLODAP). *Global Biogeochemical Cycles* **18** (2004).
2. Weaver, A. J. et al. The UVic Earth System Climate Model: Model description, climatology, and applications to past, present and future climates. *Atmosphere-Ocean* **39**, 361-428 (2001).
3. Menviel, L., Timmermann, A., Mouchet, A. & Timm, O. Meridional reorganizations of marine and terrestrial productivity during Heinrich events. *Paleoceanography* **23** (2008).
4. Meissner, K. J., Schmittner, A., Weaver, A. J. & Adkins, J. The ventilation of the North Atlantic Ocean during the Last Glacial Maximum: A comparison between simulated and observed radiocarbon ages. *Paleoceanography* **18**, doi:10.1029/2002PA000762 (2003).
5. Pelletier, G., Lewis, E. & Wallace, D. *A calculator for the CO_2 system in seawater for Microsoft Excel/VBA* (Washington State Department of Ecology, Olympia, WA, Brookhaven National Laboratory, Upton, NY, 2005).
6. Mehrbach, C., Culberso, C. H., Hawley, J. E. & Pytkowic, R. M. Measurement of apparent dissociation-constants of carbonic-acid in seawater at atmospheric-pressure. *Limnology and Oceanography* **18**, 897-907 (1973).
7. Dickson, A. G. Thermodynamics of the dissociation of boric-acid in synthetic seawater from 273.15K to 318.15K. *Deep-Sea Research Part A-Oceanographic Research Papers* **37**, 755-766 (1990).
8. Lee, K. et al. The universal ratio of boron to chlorinity for the North Pacific and North Atlantic oceans. *Geochimica et Cosmochimica Acta* **74**, 1801-1811 (2010).
9. Broecker, W. & Peng, T. H. *Tracers in the Sea* (Lamont Doherty Geological Observatory, 1982).
10. Zeebe, R. E. & Wolf-Gladrow, D. A. *CO_2 in Seawater: Equilibrium, Kinetics, Isotopes* (ed. Halpern, D.) (Elsevier, Amsterdam, 2001).
11. Rae, J. W. B., Foster, G. L., Schmidt, D. N. & Elliott, T. Boron isotopes and B/Ca in benthic foraminifera: Proxies for the deep ocean carbonate system. *Earth and Planetary Science Letters* **302**, 403-413 (2011).
12. Boyle, E. & Keigwin, L. D. Comparison of Atlantic and Pacific paleochemical records for the Last 215,000 years: Changes in deep ocean circulation and chemical inventories. *Earth and Planetary Science Letters* **76**, 135-150 (1985/86).
13. Yu, J. M., Elderfield, H., Greaves, M. & Day, J. Preferential dissolution of benthic foraminiferal calcite during laboratory reductive cleaning. *Geochemistry Geophysics Geosystems* **8**, Q06016, doi:10.1029/2006GC001571 (2007).
14. Barker, S., Greaves, M. & Elderfield, H. A study of cleaning procedures used for foraminiferal Mg/Ca paleothermometry. *Geochemistry Geophysics Geosystems* **4**, 8407 (2003).

15. Yu, J. M., Day, J., Greaves, M. & Elderfield, H. Determination of multiple element/calcium ratios in foraminiferal calcite by quadrupole ICP-MS. *Geochemistry Geophysics Geosystems* **6**, Q08P01, doi:10.1029/2005GC000964 (2005).
16. Broecker, W., Yu, J. & Putnam, A. E. Two contributors to the glacial CO_2 decline. *Earth and Planetary Science Letters*, http://dx.doi.org/10.1016/j.epsl.2015.07.019 (2015).
17. Rosenthal, Y., Boyle, E. A. & Slowey, N. Temperature control on the incorporation of magnesium, strontium, fluorine, and cadmium into benthic foraminiferal shells from Little Bahama Bank: Prospects for thermocline paleoceanography. *Geochimica et Cosmochimica Acta* **61**, 3633-3643 (1997).
18. Broecker, W. & Clark, E. A dramatic Atlantic dissolution event at the onset of the last glaciation. *Geochemistry Geophysics Geosystems* **2**, art. no.-2001GC000185 (2001).
19. Bickert, T. & Mackensen, A. in *The South Atlantic in the Late Quaternary: Reconstruction of material budgets and current systems* (eds. Wefer, G., Mulitza, S. & Ratmeyer, V.) 671-692 (Springer-Verlag, New York, 2003).
20. Howard, W. R. & Prell, W. L. Late Quaternary $CaCO_3$ production and preservation in the Southern Ocean - Implications for oceanic and atmospheric carbon cycling. *Paleoceanography* **9**, 453-482 (1994).
21. Hodell, D. A., Venz, K. A., Charles, C. D. & Ninnemann, U. S. Pleistocene vertical carbon isotope and carbonate gradients in the South Atlantic sector of the Southern Ocean. *Geochemistry Geophysics Geosystems* **4**, doi:10.1029/2002GC000367 (2003).
22. Sachs, J. & Anderson, R. F. Increased productivity in the subantarctic ocean during Heinrich events. *Nature* **434**, 1118-1121 (2005).
23. Yu, J. M. & Elderfield, H. Benthic foraminiferal B/Ca ratios reflect deep water carbonate saturation state. *Earth and Planetary Science Letters* **258**, 73-86, doi: 10.1016/j.epsl.2007.03.025 (2007).
24. Yu, J., Anderson, R. F. & Rohling, E. J. Deep ocean carbonate chemistry and glacial-interglacial atmospheric CO_2 changes. *Oceanography* **27**, 16-25 (2014).
25. Yu, J. et al. Responses of the deep ocean carbonate system to carbon reorganization during the Last Glacial–interglacial cycle. *Quaternary Science Reviews* **76**, 39-52 (2013).
26. Raitzsch, M., Hathorne, E. C., Kuhnert, H., Groeneveld, J. & Bickert, T. Modern and late Pleistocene B/Ca ratios of the benthic foraminifer Planulina wuellerstorfi determined with laser ablation ICP-MS. *Geology* **39**, 1039-1042 (2011).
27. Brown, R. E., Anderson, L. D., Thomas, E. & Zachos, J. C. A core-top calibration of B/Ca in the benthic foraminifers Nuttallides umbonifera and Oridorsalis umbonatus: A proxy for Cenozoic bottom water carbonate saturation. *Earth and Planetary Science Letters* **310**, 360-368 (2011).
28. Yu, J. M., Elderfield, H. & Piotrowski, A. Seawater carbonate ion-$\delta^{13}C$ systematics and application to glacial-interglacial North Atlantic ocean circulation. *Earth and Planetary Science Letters* **271**, 209-220. doi:10.1016/j.epsl.2008.04.010 (2008).
29. Grant, K. M. et al. Rapid coupling between ice volume and polar temperature over the past 150,000 years. *Nature*, doi:10.1038/nature11593 (2012).
30. Lisiecki, L. E. & Raymo, M. E. A Pliocene-Pleistocene stack of 57 globally distributed benthic $\delta^{18}O$ records. *Paleoceanography* **20**, PA1003, doi:10.1029/2004PA001071 (2005).
31. Ninnemann, U. S. & Charles, C. D. Changes in the mode of Southern Ocean circulation over the last glacial cycle revealed by foraminiferal stable isotopic variability. *Earth And Planetary Science Letters* **201**, 383-396 (2002).
32. Bickert, T. & Wefer, G. South Atlantic and benthic foraminifer delta C-13 deviations: implications for reconstructing the Late Quaternary deep-water circulation. *Deep-Sea Research Part Ii-Topical Studies in Oceanography* **46**, 437-452 (1999).
33. Rohling, E. J. et al. Sea-level and deep-sea-temperature variability over the past 5.3 million years. *Nature* **508**, 477-+ (2014).
34. Sarmiento, J. L. & Gruber, N. *Ocean Biogeochemical Dynamics* (Princeton University, Princeton, 2006).
35. Broecker, W. S. & Peng, T. H. The role of $CaCO_3$ compensation in the glacial to interglacial atmospheric CO_2 change. *Global Biogeochemical Cycles* **1**, 15-29 (1987).
36. Boyle, E. The role of vertical chemical fractionation in controlling late Quaternary atmospheric carbon dioxide. *J. Geophys. Res.* **93**, 15701-15714 (1988).
37. Sigman, D. M., McCorkle, D. C. & Martin, W. R. The calcite lysocline as a constraint on glacial/interglacial low-latitude production changes. *Global Biogeochemical Cycles* **12**, 409-427 (1998).
38. Chikamoto, M. O., Matsumoto, K. & Ridgwell, A. Response of deep-sea CaCO3 sedimentation to Atlantic meridional overturning circulation shutdown. *Journal of Geophysical Research-Biogeosciences* **113** (2008).

39. Emerson, S. & Archer, D. Glacial carbonate dissolution cycles and atmospheric pCO_2: A view from the ocean bottom. *Paleoceanography* **7**, 319-331 (1992).
40. Gibbs, M. T. & Kump, L. R. Global chemical erosion during the last glacial maximum and the present: Sensitivity to changes in lithology and hydrology. *Paleoceanography* **9**, 529-543 (1994).
41. Menviel, L. & Joos, F. Toward explaining the Holocene carbon dioxide and carbon isotope records: Results from transient ocean carbon cycle-climate simulations. *Paleoceanography* **27** (2012).
42. Anderson, R. F., Fleisher, M. Q., Lao, Y. & Winckler, G. Modern $CaCO_3$ preservation in equatorial Pacific sediments in the context of late-Pleistocene glacial cycles. *Marine Chemistry* **111**, 30-46. doi:10.1016/j.marchem.2007.11.011 (2008).
43. Archer, D. A data-driven model of the global calcite lysocline. *Global Biogeochemical Cycles* **10**, 511-526 (1996).
44. Meissner, K. J., McNeil, B. I., Eby, M. & Wiebe, E. C. The importance of the terrestrial weathering feedback for multimillennial coral reef habitat recovery. *Global Biogeochemical Cycles* **26** (2012).
45. Goosse, H. et al. Description of the Earth system model of intermediate complexity LOVECLIM version 1.2. *Geoscientific Model Development* **3**, 603-633 (2010).
46. Menviel, L., England, M. H., Meissner, K. J., Mouchet, A. & Yu, J. Atlantic-Pacific seesaw and its role in outgassing CO2 during Heinrich events. *Paleoceanography* **29**, 58-70 (2014).
47. Saenko, O. A., Schmittner, A. & Weaver, A. J. The Atlantic-Pacific seesaw. *Journal of Climate* **17**, 2033-2038 (2004).
48. Schmittner, A., Oschlies, A., Matthews, H. D. & Galbraith, E. D. Future changes in climate, ocean circulation, ecosystems, and biogeochemical cycling simulated for a business-as-usual CO2 emission scenario until year 4000 AD. *Global Biogeochemical Cycles* **22** (2008).
49. Kwon, E. Y. et al. North Atlantic ventilation of "southern-sourced" deep water in the glacial ocean. *Paleoceanography* **27** (2012).
50. Menviel, L., Spence, P. & England, M. H. Contribution of enhanced Antarctic Bottom Water formation to Antarctic warm events and millennial-scale atmospheric CO2 increase. *Earth and Planetary Science Letters* **413**, 37-50 (2015).
51. Yu, J. et al. Deep South Atlantic carbonate chemistry and increased interocean deep water exchange during last deglaciation. *Quaternary Science Reviews* (2014).
52. Mackensen, A., Hubberten, H.-W., Bickert, T., Fischer, G. & Fütterer, D. K. The $\delta^{13}C$ in benthic foraminiferal tests of *Fontbotia wuellerstorfi* (schwager) relative to the $\delta^{13}C$ of dissolved inorganic carbon in Souther Ocean deep water: Implications for glacial ocean circulation models. *Paleoceanography* **8**, 587-610 (1993).
53. Oppo, D., Fairbanks, R. G., Gordon, A. L. & Shackleton, N. J. Late Pleistocene Southern Ocean $\delta^{13}C$ variability. *Paleoceanography* **5**, 43-54 (1990).
54. Curry, W. B. (2004).
55. Thomson, J. et al. Implications for sedimentation changes on the Iberian margin over the last two glacial/interglacial transitions from (Th-230(excess))(0) systematics. *Earth and Planetary Science Letters* **165**, 255-270 (1999).
56. Curry, W. B. Late Quaternary deep circulation in the western equatorial Atlantic. *South Atlantic*, 577-598 (1996).
57. McManus, J. F., Francois, R., Gherardi, J. M., Keigwin, L. D. & Brown-Leger, S. Collapse and rapid resumption of Atlantic meridional circulation linked to deglacial climate changes. *Nature* **428**, 834-837 (2004).
58. Bohm, E. et al. Strong and deep Atlantic meridional overturning circulation during the last glacial cycle. *Nature* **517**, 73-U170 (2015).
59. Oliver, K. I. C. et al. A synthesis of marine sediment core delta C-13 data over the last 150 000 years. *Climate of the Past* **6**, 645-673 (2010).
60. Lea, D. W. A Trace-Metal Perspective On The Evolution Of Antarctic Circumpolar Deep-Water Chemistry. *Paleoceanography* **10**, 733-747 (1995).
61. Lea, D. W. & Boyle, E. A. A 210,000-year record of barium variability in the deep Northwest Atlantic-Ocean. *Nature* **347**, 269-272 (1990).